Effect of Crystalline Phase and Facet Nature on the Adsorption of Phosphate Species onto TiO2 Nanoparticles

Rémi Bérard, Capucine Sassoye, Hélène Terrisse, Patricia Bertoncini, Bernard Humbert, Sophie Cassaignon, Sophie Le Caër

Effect of Crystalline Phase and Facet Nature on the Adsorption of Phosphate Species onto TiO_2 Nanoparticles

Rémi Bérard,[1,2] Capucine Sassoye,[2] Hélène Terrisse,[3] Patricia Bertoncini,[3] Bernard Humbert,[3] Sophie Cassaignon,[2] and Sophie Le Caër[1*]

[1]*NIMBE, CEA, CNRS, Université Paris-Saclay, CEA Saclay, 91191 Gif sur Yvette Cedex, France*

[2]*Sorbonne Université, CNRS, Laboratoire Chimie de la Matière Condensée de Paris, LCMCP, UMR 7574, 4 Place Jussieu, 75005 Paris, France*

[3]*Nantes Université, CNRS, Institut des Matériaux de Nantes Jean Rouxel, IMN, UMR 6502, 2 rue de la Houssinière, 44000 Nantes, France*

**corresponding author: sophie.le-caer@cea.fr*

ABSTRACT

The current use of TiO_2 nanoparticles raises questions about their impact on our health. Cells interact with these nanoparticles via the phospholipid membrane and, in particular, the phosphate head. This highlights the significance of understanding the interaction between phosphates and nanoparticles possessing distinct crystalline structures, specifically anatase and rutile. It is crucial to determine whether this adsorption varies based on the exposed facet(s). Consequently, various nanoparticles of anatase and rutile TiO_2, characterized by well-defined morphologies, were synthesized. In the case of the anatase samples, bipyramids, needles and cubes were obtained. For the rutile samples, all exhibited a needle-like shape, featuring {110} facets along the long direction of the needles and facets {111} on the upper and lower parts. Phosphate adsorption experiments carried out at pH 2 revealed that the maximum adsorption was relatively consistent across all samples, averaging around 1.5 phosphate.nm^{-2} in all cases. Experiments using infrared spectroscopy on dried TiO_2 powders showed that phosphates were chemisorbed on the surfaces and that the mode of adsorption depended on the crystalline phase and the nature of the facet: the anatase phase favors bidentate adsorption more than the rutile crystalline phase.

INTRODUCTION

TiO_2 nanoparticles are used in a wide range of applications due to their bandgap energy value (around 3.2 eV), which allows them to be excited by the UV radiation from sunlight.[1,2] Specifically, they are employed in photocalysis,[3–8] decontamination processes, self-cleaning materials and photovoltaics.[9] Moreover, TiO_2 nanoparticles serve as white pigments in paints, cosmetics[10] and foods,[11] as in the food additive E171[12–14]. The significant presence of these nanoparticles in the environment has thus raised concerns about their effects on the environment and human health.[2,15,16] Notably, several studies have suggested a potential correlation between cancers and the exposure of TiO_2 nanoparticles.[17] Consequently, in 2015, the French Agency for Food, Environmental and Occupational Health and Safety (ANSES) defended to European institutions for classifying TiO_2 nanoparticles as a class 1-B carcinogen. It concluded in 2017 that any product containing TiO_2 nanoparticles, whatever its form, should be classified as a class 2 carcinogen when inhaled. In 2017, a study on rats further showed a potential involvement of the food additive E171 in colorectal cancer development.[17] In response, the French government banned the use of E171 in food pending further investigations into its health effects. This prohibition has been annually extended since 2019.[18]

Understanding the precise mechanisms through which TiO_2 impacts health remains challenging, particularly when considering the various sizes, morphologies and shapes of nanoparticles.[19,20] Generally, the effects of TiO_2 nanoparticles on organisms are attributed to the formation of radical oxidizing species (ROS) capable of damaging the organelles or DNA of an organism's cells.[21,22] Given this mechanism, the interaction between nanoparticles and living organisms becomes a fundamental issue when considering TiO_2's health implications. In the case of cells, the initial contact is through the phospholipid membrane. A study has highlighted the phospholipids ability to interact with TiO_2 nanoparticles,[23] suggesting that the phosphate head, directly present on the surface membrane, may play a particular role in adsorption mechanisms. Consequently, understanding the adsorption of phosphate species onto TiO_2 nanoparticles becomes of paramount importance and we can expect this adsorption phenomenon to be directly influenced by the shape of the nanoparticles, their crystalline facets and their environment. Hiji *et al.*[24] described the relationship between phosphate adsorption and TiO_2 rutile facets, and showed that the {001} rutile facet kinetically favored phosphate ion adsorption compared to the other facets.

TiO_2 can be found in three main phases: rutile, anatase and brookite, each characterized by different crystalline facets. The aim of the present paper is to determine whether the adsorption of phosphate species is influenced by the morphology and crystalline nature (specifically anatase and rutile) of these nanoparticles. To ensure control over these variables, we used custom-designed nanoparticles rather than commercially available ones. This allowed us to precisely control both the crystalline phase and shape of the nanoparticles. We also worked at a pH of 2, which does not reflect physiological pH, but allowed us to optimize phosphate adsorption on nanoparticles, in order to better understand their adsorption modes.[25] Our aims are therefore: i) to synthesize well-controlled nanoparticles with similar size but varying shapes and crystallinities; ii) to evaluate the amount of phosphate species adsorbed onto these different nanoparticles; iii) to deeper characterize the nature of phosphate species adsorption. Near- and mid-infrared spectroscopy were used to achieve these objectives. This approach provides valuable insights into the surface hydroxyl groups of TiO_2 and their interaction with phosphate species.

EXPERIMENTAL SECTION

1. TiO_2 nanoparticles synthesis

Anatase and rutile TiO_2 nanoparticles were synthesized by adapting existing protocols.[8,9,26–30] Synthesis of the nanoparticles is detailed in the SI. Six different types of nanoparticles (noted A-shape for anatase and R-shape for rutile) were produced using well-controlled synthesis methods. Six different samples were made: three anatase, labelled as A-Bipy (anatase bipyramids), A-Rod (anatase rods), A-Cube (anatase cubes) and three rutile rods of different sizes (R-Small, R-Mid and R-Long).

2. Characterization of the nanoparticles

2.1. *X-Ray Diffraction (XRD) measurements*

Phase crystallinity and powder purity were determined by X-ray diffraction. The patterns were measured with a Bruker D8 X-ray diffractometer operating in the Bragg–Brentano reflection mode equipped with a nickel filter to select the Cu-$K_{\alpha 1,2}$ radiations. The data were collected in the 2θ = 10–120° range with 0.02° steps. Analysis was performed in fixed-slit mode. Phase assignment was performed using PDF files from powder diffraction files (ICDD, PDF4+) of anatase (00-021-1272), rutile (00-021-1276) and brookite (00-029-1360). We have also used the Scherrer equation that provides access to the mean coherence domain of particles.

This value gives insight into the size of the particles when they are relatively monodisperse and monocrystalline. Particle sizes were estimated in the direction normal to the planes shown in Table 1. We used a classical form factor of 0.9.

2.2. *Electron microscopy characterization*

Transmission electron microscopy (TEM) images were obtained on a FEI Tecnai Spirit G2 instrument at an acceleration voltage of 120 kV. The nanoparticles were ultrasonicated in water and dispersed on carbon-covered Cu grids. At least 200 particles were measured on TEM images to determine their size.

To study the crystal planes, we used Nant'Themis' HRSTEM facility. Scanning transmission electron microscopy (STEM) experiments were performed on a probe-corrected Themis Z G3 microscope (Thermo Fisher Scientific) equipped with a High Angle Annular Dark Field (HAADF) detector, a four-quadrant annular detector (DF4) dedicated to Differential Phase Contrast (DPC) imaging. DPC-STEM and HAADF-STEM images of the particles were obtained using an acceleration voltage of 300 kV, a beam convergence angle of 13.3 mrad, an electron beam-current of 10 pA and a camera length of 360 mm. The DF4 detector collection angle was set to 4-16 mrad and the HAADF collection angle to 16-100 mrad. For DPC imaging, four images used for 2D integration were acquired by the DF4 detector with an optional high-pass filter applied to reduce the low-frequency information in the integrated-DPC (i-DPC) images. 25 µL of a 20 $mg.L^{-1}$ dispersion of samples containing a known amount of phosphate species were deposited on a lacey carbon gold TEM grid and let dry.

2.3. *Specific surface (BET) measurement*

Precise amounts of each sample were degassed at 90°C under 20 mTorr (Vac Prep 061, Micromeritics®). The sample was then degassed at 150°C for 17 h at 20 mTorr (3-Flex, Micromeritics®). The Brunauer-Emmett-Teller (BET) surface area analysis was carried out using nitrogen (N_2) as the adsorbed gas.

2.4. *Zeta potential measurement*

For each nanoparticle suspension, a predetermined amount was dispersed with a 0.01 $mol.L^{-1}$ NaCl solution to obtain a TiO_2 concentration of 0.15 $g.L^{-1}$. The resulting dispersion was sonicated for 15 min (Elmasonic P, 100 W, 37 Hz, sweep mode). Zeta potential measurements were carried out for different pH values ranging from 2 to 10. Solutions of HCl (0.1 and 0.01 $mol.L^{-1}$) and NaOH (0.001 $mol.L^{-1}$) were thus prepared by maintaining a constant

NaCl concentration of 0.01 mol.L^{-1}. Consequently, the final TiO_2 concentration was 0.05 g.L^{-1}. To prevent carbonation, pH of the solutions was adjusted in a glovebox under N_2. The measurements were then performed outside the glovebox using a Zetasizer Nano-ZS (Malvern Instrument). Prior to analysis, each closed vial was sonicated independently (Elmasonic P, 100 W, 37 Hz, sweep mode) for 5 min. A minimum of two samples from each vial were analyzed, at least three times each. We used Smoluchowski approximation to convert electrophoretic mobility to zeta potential. Reported values correspond to the averages of the recorded data points. Measurements were systematically repeated several times to ensure data reproducibility.

3. Phosphate species adsorption isotherms

The described protocol is an adaptation of the one described in reference [25]. To perform phosphate adsorption isotherms, TiO_2/phosphate samples were first prepared. All measurements were carried out at pH = 2 to minimize the undesirable carbonates adsorption on the surface of nanoparticles and maximize phosphate adsorption. At this pH value, H_3PO_4 and $H_2PO_4^-$ exist at comparable concentration. Even if dihydrogen phosphate anion may adsorb preferentially to the surface of the nanoparticles, since the TiO_2 surface is positively charged at this pH, H_3PO_4 can also adsorb.[31] We therefore refer to phosphate species in the following text. Note also that in the rest of the experimental protocol, the given values correspond to the total amount of phosphate species in solution.

For isotherm adsorption experiments, we only worked with the TiO_2 dispersions. The initial mass concentration was assessed by centrifugation and oven drying at 45°C. The pH of the solutions was set at 2, and the NaCl concentration was fixed at 0.01 mol.L^{-1}. A 0.05 mol. L^{-1} phosphate solution was also prepared by using Na_2HPO_4 (Sigma Aldrich, ReagentPlus®, 99.0%). The desired amount of phosphate was then added to the TiO_2 dispersion. The tubes were then rotated at 25 rpm, at 25°C for at least 24 h to ensure complete adsorption onto the TiO_2 nanoparticles. Typical TiO_2 concentrations varied between 3.5 mg.mL^{-1} and 6 mg.mL^{-1} depending on the experiment.

The tubes were centrifuged (40000 g, 1h30) and the supernatant was carefully separated from the precipitated nanoparticles. The quantity of phosphates adsorbed on the TiO_2 surface was determined by comparing the quantity of species remaining in the final supernatant with those initially added to each tube. The total phosphate concentration in the supernatant was carried out using an adapted quantitative UV-Vis protocol using a combined molybdenum reagent that forms a blue compound with phosphate species[32] absorbing at 824 nm (ε:

517 ± 15 $L.mol^{-1}.cm^{-1}$). The reagent was prepared as follows: six volumes of a 0.42 % solution of ammonium molybdate tetrahydrate (Sigma Aldrich, ≥ 99.0 %) in 0.5 $mol.L^{-1}$ sulfuric acid (prepared from Merck, EMSURE®, 98 %) was mixed with one volume of a 10% L-ascorbic acid solution (Sigma Aldrich, 99 %). Phosphate standards were prepared by diluting different amounts of the 0.5 $mol.L^{-1}$ phosphate. 60 µL of the solutions to be measured (supernatant or standard) were mixed with 2.1 mL of the combined reagent and 900 µL of 1 M HCl. The tubes thus prepared were placed in a bath at 45°C for around 40 min, until the solutions took on a stable blue color. Absorption spectra were then measured between 300 and 900 nm using a UV-Visible spectrometer (UV-2550, Shimadzu) with a PMMA cell of 1 cm of optical path.

More details about this protocol can be found in the SI, together with evaluation of uncertainties.

The TiO_2 wet powders obtained after centrifugation (see above) were retained for analysis by infrared spectroscopy.

4. Characterization of the surface of the nanoparticles by infrared spectroscopy

4.1. *Diffuse Reflectance Infrared Fourier Transform Spectroscopy (DRIFT)*

Working in the near-infrared (NIR) range has several advantages for studying/monitoring the status of adsorbed or structural water molecules: (i) this range allows us to work with pure mineral powders without any need for dilution in a non-absorbing matrix;[33] (ii) it provides a quantitative analysis that is not obtained in the mid-IR region; (iii) in the case of oxides and clay materials, in the mid-IR range, it is often difficult to determine unambiguously the position of OH stretching bands of adsorbed water,[34] whereas in the Near-IR range, the spectral separation between structural and water OH groups is increased, allowing for easier and more precise band assignments.

Diffuse Reflectance Fourier Transform Infrared spectroscopy (DRIFTS) was performed using a Bruker Vertex 70 spectrometer equipped with a Praying Mantis configuration (Harrick Scientific Products Inc.). The reflectance spectra are displayed in $-\log(R/R_0)$, where R corresponds to the diffuse reflection collected on the sample and R_0 to the reflection recorded on a reference material. Here, an aluminum mirror was used to minimize any signal of adsorbed water molecules on the reference. Via a slow sweep of dry air, the sample chamber was taken from ambient relative humidity to less than 2% at approximately 298 K, making it possible to preserve the sample powders from excessive physical variations. The wet powder recovered during isotherm preparation was used for the measurements. Due to the small amount of powder

(approximately 6 mg per isotherm point), a mixture of three isotherm points was required for analysis. The samples were placed in the analysis chamber under the flow of dry air for early dehydration. Following the dehydration process, spectra were recorded in the MIR and NIR spectral regions between 6000 cm^{-1} and 1200 cm^{-1} with a resolution of 4 cm^{-1} using a DTGS detector. After confirmation of maximum dehydration (when no more spectral evolution is observed), the final spectra were recorded. The spectra shown here result from the accumulation of 800 scans.

Moreover, to obtain reliable data below 1200 cm^{-1}, we also carried out transmission experiments with samples diluted in KBr (Sigma-Aldrich, FT-IR grade, ≥99%) pellets (see below).

4.2. *Transmission Fourier Transform Infrared Spectroscopy (FT-IR)*

Mid-infrared spectra between 4000 cm^{-1} and 370 cm^{-1} were also recorded using a Bruker Vertex 70 apparatus with a DTGS detector. 1% (mass) of the sample was dispersed in KBr, pelletized into self-supporting discs using a pressure of 10^9 Pa, and then placed in the spectrometer. The choice of this dilution ensured that the most intense bands were not saturated. It was also perfectly suited to our samples, which were available in limited quantities. The resolution was set at 4 cm^{-1} and each spectrum was an average of 100 scans. The KBr background was subtracted in all cases.

RESULTS AND DISCUSSION

1. TiO_2 nanoparticles characterization

1.1. Characterization of the crystalline phases

To confirm the crystallographic structure of each powder, XRD analyses were performed (Figure 1). In each case, the observed crystallographic phase was as expected. A small amount of brookite phase was observed in rutile synthesized hydrothermally for one month (R-Long). Similarly, traces of brookite were also observed in the bipyramids (A-Bipy) and rods (A-Rod) of anatase structure. The relative abundance between brookite and the other phases was estimated using the ratios of the peak areas corresponding to (121) brookite, (110) rutile and (200) anatase respectively, taking into account the relative contribution of each peak to its

single-phase profile. Brookite accounts for approximately 3% of the phase in the R-Long sample, 1% in A-Rod and 8% in A-Bipy. It is therefore considered negligible.

A slight peak shift towards smaller angles was also observed for the rutile R-Small (Figure 1). This was previously attributed to the distortion and expansion of the quadratic rutile cell (b = 4.674 Å instead of 4.593 Å) by Cassaignon *et al.*[29]

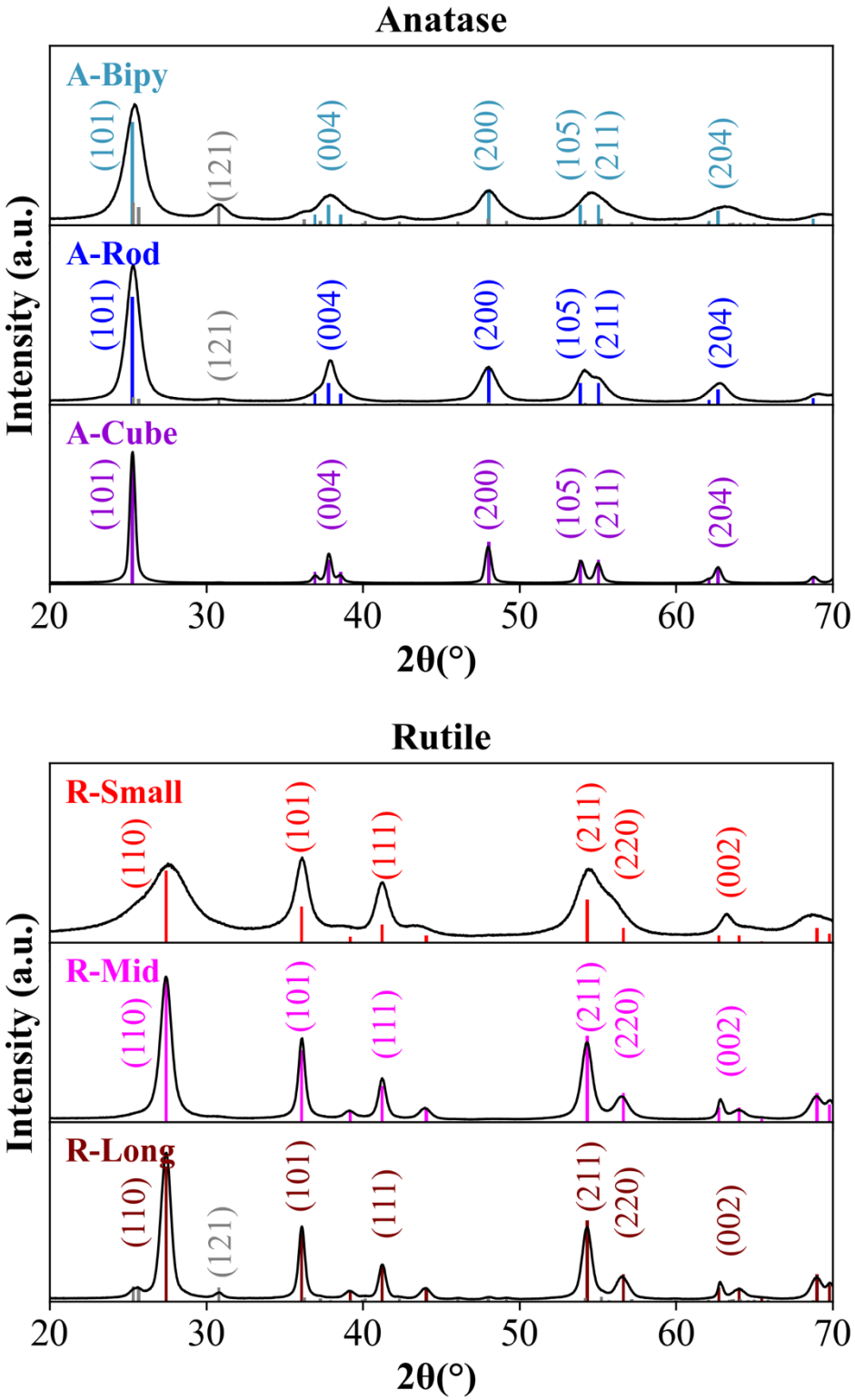

Figure 1. *XRD patterns for each type of TiO_2 nanoparticles synthesized. The bars represent the peaks obtained from the powder diffraction files for anatase (ICCD: 00-021-1272), rutile (ICCD: 00-021-1276) and brookite (grey, ICCD: 00-029-1360).*

1.2. Morphology and size of the nanoparticles

Sample size, and therefore specific surface area, plays an important role in understanding adsorption phenomena. A first approximation of nanoparticle size was made using the Scherrer formula (Table 1). In addition, TEM images are shown in Figure 2. The corresponding sizes obtained from both techniques are reported in Table 1. The observed morphologies are as expected. Detailed size distribution for length and width, based on TEM images, is given in Figures S1 and S2 for the anatase and rutile structures, respectively.

Concerning the anatase samples, some sharp edges in the case of A-Bipy can be distinguished and are consistent with a bipyramidal structure. Rods (or elongated bipyramids) are observed in A-Rod. TEM images reveal squares (or ovoid shapes) in the case of A-Cube. For A-Bipy and A-Rod, the specific surface area measured by BET is around 200 $m^2.g^{-1}$ (Table 1). This surface is clearly smaller in the case of A-Cube (67 $m^2.g^{-1}$, see Table 1), consistent with its larger size. Estimated specific surface areas using the sizes measured by TEM (see Figure S1 and Table S1 in SI) corroborate well with the BET data. Overall, both XRD and TEM data lead to similar nanoparticles sizes for anatase samples.

In the case of rutile samples, there are significant differences between the sizes of the Scherrer domains obtained from the XRD data and microscopy measurements. Direct microscopy measurements of needle-shaped objects are certainly more accurate. Indeed, Sherrer's formula attributes the broadening of the peaks to the decrease in crystal domain size alone. Given the asymmetry and broadening of the diffraction peaks, it is difficult to take strain into account. Overall, R-Long needles are bigger than R-Mid, that are bigger than R-Small sample. As expected, this leads to a higher specific surface area (212 $m^2.g^{-1}$) than in R-Long (82 $m^2.g^{-1}$) or R-Mid (79 $m^2.g^{-1}$) (Table 1). In this latter case, this low value might be explained by needles aggregation (bundles) limiting accessible surfaces.

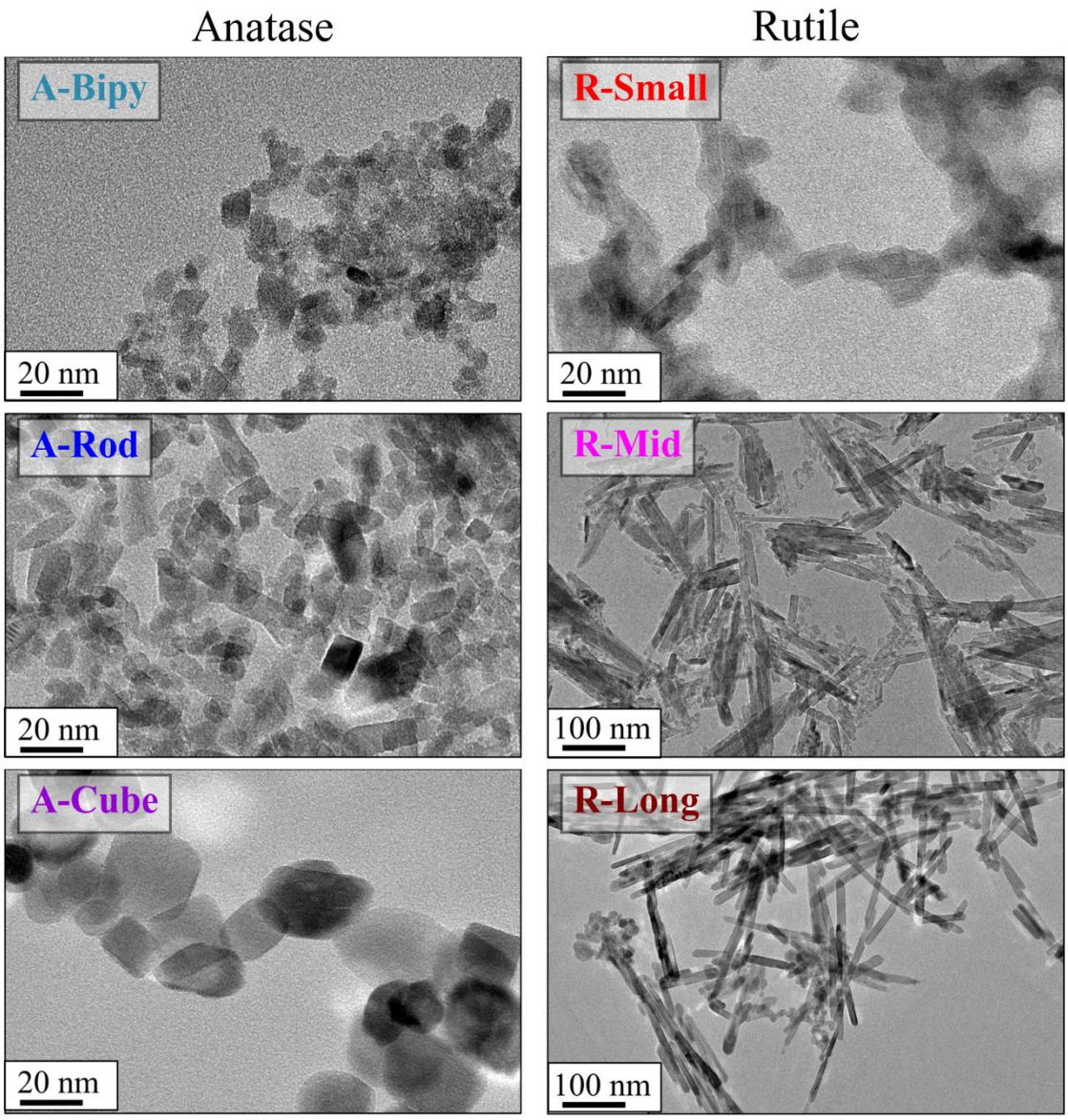

Figure 2. *TEM images of the different samples.*

Table 1. *Characterization of the synthesized nanoparticles. XRD data (Scherrer formula) give the crystallite size perpendicularly to the crystallographic planes while TEM images give mean distances for the different TiO_2 nanoparticles with standard error. Roughly estimated specific surface areas, calculated from average sizes obtained by TEM analysis, are given in Table S1. The anisotropic ratio (length/width) is specified in parentheses for TEM size. Specific surface areas were measured by BET analysis. The isoelectric point (IEP) values are also reported (see the zeta potential measurement section).*

	Anatase									Rutile								
	A-Bipy			A-Rod			A-Cube			R-Small			R-Mid			R-Long		
Scherrer (nm)	(101)	(004)	(200)	(101)	(004)	(200)	(101)	(004)	(200)	(110)	(101)	(111)	(110)	(101)	(002)	(110)	(101)	(002)
	6	5	5	8	12	7	22	24	22	2	9	9	10	19	25	12	21	30
TEM (nm)	8(±0.3) x 6(±0.2) (1.3)			16(±0.4) x 7(±0.1) (2.3)			25(±0.3) x 21(±0.3) (1.2)			17(±0.6) x 6(±0.2) (2.8)			41(±2.4) x 9(±0.2) (4.6)			66(±2.2) x 13(±0.1) (5.0)		
BET (m^2/g)	240 ± 5			181 ± 5			67 ± 5			212 ± 5			79 ± 5			82 ± 5		
IEP	6.4			6.5			5.5			5.6			6.1			5.6		

1.3. O-H sites on the various samples

In order to gain a detailed understanding of the chemical bonds present in/on the nanoparticles, the DRIFT spectra of the different types of TiO_2 were recorded between 6000 and 1200 cm^{-1} (see Figure S3 for the overall spectra). Figure 3 exhibits the region between 3575 cm^{-1} and 3760 cm^{-1}, characteristic of the stretching modes of the surface O-H bonds. The band assignments are given in Table 2 (μ_1-OH represents a hydroxyl group coordinated to an unique surface titanium atom; μ_2-OH corresponds to a bi-coordinated hydroxyl group and μ_1-OH_2 represents a chemisorbed water molecule).

It is noteworthy that the global spectra (Figure S3) evidence the presence of organic species on the A-Cube anatase particles due to the use of surfactant during synthesis. Thus, the meticulous washing protocol does not completely eliminate these species,[8] potentially influencing the cubes' surface reactivity.

For anatase, insights from both DFT and experimental work by Arrouvel et al.[35] and Dzwigaj et al.[36] give indications about OH groups on specific nanoparticle facets. In what follows, IV, V and VI refer to quadra, penta and hexa-coordinated titanium atoms. Following Arrouvel's work, the observed bands at 3725 and 3736 cm^{-1} are attributed to the O-H stretching modes of Ti_V-μ_1-OH groups on {110} and {001} facets, respectively (3730-3742 and 3725 cm^{-1} in their referenced experimental bands[37–40]). Similarly, the band near 3683 cm^{-1} is attributed to a stretching O-H mode of Ti_{VI}-μ_1-OH groups on {100} facet (3690 cm^{-1} in their referenced experimental bands[37]). Finally, the band detected around 3636 cm^{-1} is attributed to Ti_{VI}-μ_1-OH_2 streching modes on {101} facets (observed between 3620 and 3680 cm^{-1} in their referenced experimental bands[37–41]).

In the case of rutile-type samples, Kipreos *et al.* have studied the evolution of the bands after deuteration and distinguished terminal μ_1-OH from bridging μ_2-OH hydroxyls.[42] The authors attributed the bands detected at around 3725 cm^{-1} and 3680 cm^{-1} to Ti_V-μ_1-OH and Ti_{IV}-μ_1-OH respectively.[42] In the present work, all rutile samples present a band near 3725 cm^{-1}, suggesting a similar attribution. The bands around 3680 cm^{-1} are attributed to Ti_{IV}-μ_1-OH modes with unsaturated titanium sites for the three samples. For R-small, the band near 3650 cm^{-1} corresponds to μ_2-OH. For R-Mid and R-Long, the band around 3635 cm^{-1} can be attributed to μ_2-OH located on different planes from those absorbing around 3650 cm^{-1}.[42]

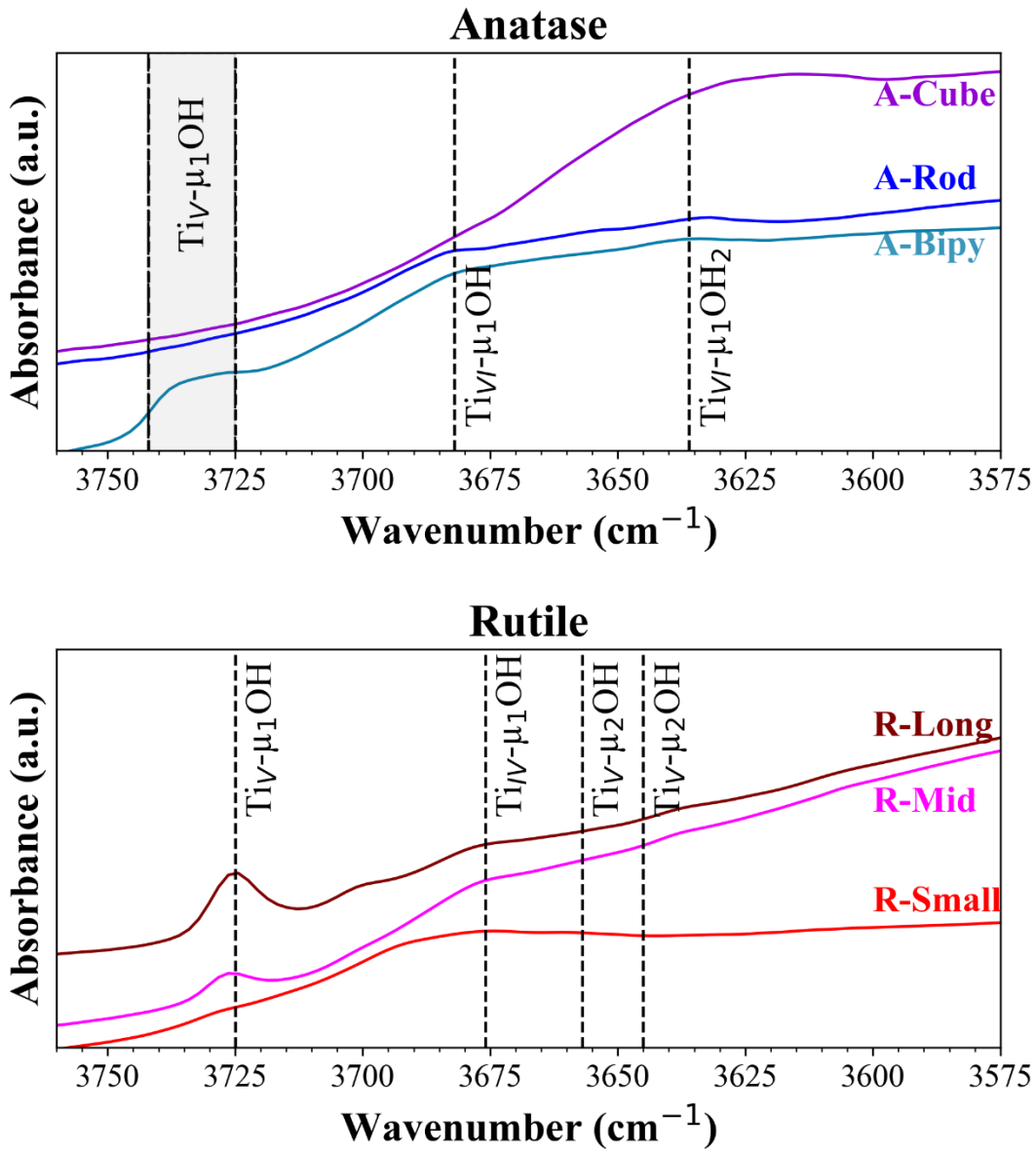

***Figure* 3.** *Zoom in on the O-H stretching band for the dehydrated anatase and rutile samples (see Figure S3 for the global spectra). The various stretching modes observed are listed in Table 2, along with their possible assignments. They are also indicated in the figure with dotted lines.*

Table 2. *Assignment of O-H stretching bands (in cm^{-1}) for anatase and rutile sample. Anatase: modes values were experimentally obtained by Dzwigaj et al. and compared with their DFT calculations.[35] For rutile: the bands were experimentally deduced by Kipreos et al. on dried nanoparticles.[42] μ_1-OH represents a hydroxyl group where the O atom is mono-coordinated to a surface titanium atom; μ_2-OH correspond to a bi-coordinated hydroxyl group (bridging group) and μ_1-OH_2 represents a chemisorbed water molecule. IV and V refer to quadra and penta-coordinated titanium atoms.*

Anatase					**Rutile**				
Attribution[35] (cm^{-1})		A-Bipy	A-Rod	A-Cube	Attribution[42] (cm^{-1})		R-Small	R-Mid	R-Long
Ti_V-μ_1-OH[35,36,43,44]	3730-3742	3736			Ti_V-μ_1-OH	3725	3728	3727	3724
	3725	3725					3693		3700
Ti_{VI}-μ_1-OH	3690	3683	3682		Ti_{IV}-μ_1-OH (with unsaturated titanium sites)	3680	3675	3677	3677
Ti_{VI}-μ_1-OH_2	3620-3680	3636	3633	3624	Ti_V-μ_2-OH	3650	3657		
					Ti_V-μ_2-OH (on a different plane)	3644		3636	3635

1.4. Morphology of the nanoparticles (size and facets)

Knowledge of the facets in contact with the environment is crucial to understand their interaction with phosphate species. Thus, the characterizations presented above are complemented by STEM-HAADF/ iDPC images showing the orientations of the crystal planes in relation to the shape of the nanoparticles (Figure 4).

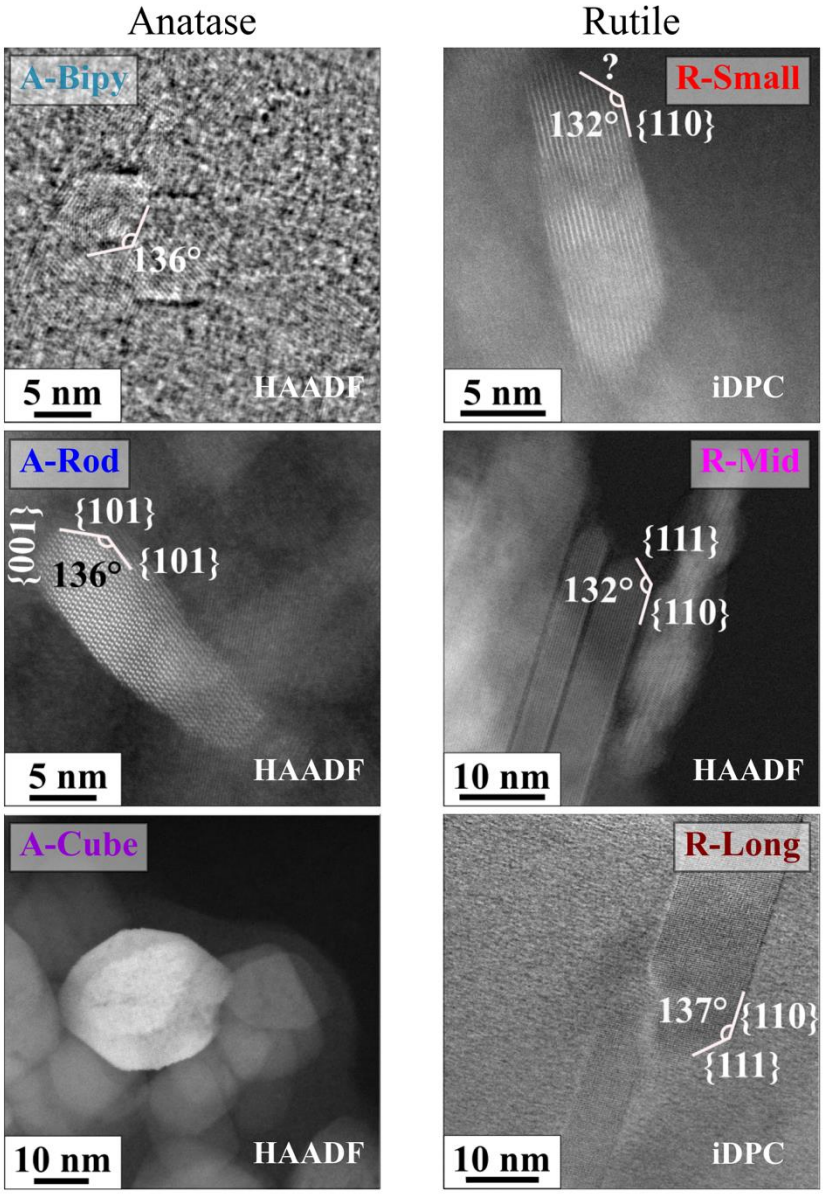

Figure 4. *High-Angle Annular Dark-Field (HAADF) or Incoherent Dark-Field Phase Contrast (iDPC) images of isolated nanoparticles from the different TiO_2 samples, with {hkl} plane assignments annotated within the images. Corresponding Fast Fourier Transform (FFT) patterns can be found in Figure S4 of the Supporting Information.*

The morphologies expected for anatase samples are bipyramids (A-Bipy), rods (A-Rod) and cubes (A-Cube), predominantly characterized by the {001}, {101} and {100} facets (Scheme 1). The {101} facet of anatase is known to be the most stable and acidic.[45,46]

Anatase samples show particularly strong aggregation between the nanoparticles (see Figure S5 in Supplementary Information). For A-Bipy (Figure 4), an angle of 136° is observed at the edge of two facets of the nanoparticles and can be attributed to the angle between two {101} facets coherent with bipyramidal structure of the nanoparticles. According to previous work,[35] the band at 3736 cm^{-1} related to terminal OH groups on the {001} surface is particularly visible for this sample, indicating the presence and importance of this facet in this sample. The shoulder at 3725 cm^{-1} could also be an indication of the existence of {110} facets. Moreover, the band at 3636 cm^{-1} can be attributed to water molecules bonded on {101} surfaces,[35] reinforcing the idea of a truncated bipyramidal structure (Scheme 1). The band at 3683 cm^{-1} could be attributed to the {100} facets and could also indicate additional truncation (not shown in the Scheme).

A-Rod sample corresponds to rods (Scheme 1). The FFT patterns (Figure S4) and the observation of the angle for a nanoparticle suggest the presence of the {101} facet. The band at 3633 cm^{-1} observed in the IR spectra (Figure 3 and Table 2) can be attributed to a water molecule bonded to a titanium atom on a {101} surface.[35] Furthermore, an additional band at 3682 cm^{-1}, can be attributed to a Ti_{VI}-μ_1-OH mode on a {100} surface.[35] We propose a model wherein rod terminations are characterized by {101} facets (Scheme 1).

For the A-Cube sample, STEM-HAADF images show ovoid morphology whereas this synthesis generally leads to cubes. Actually, this morphology corresponds to cubes with blunted edges; either ovoids are directly formed during synthesis or cube edges erosion is provoked during washing steps. This may leads to the emergence of new facets on the surface of the particles, such as {101}, {111} or {103},[36] in addition to the main {001}, {100} and {010} facets. Indeed, the broad band between 3600 cm^{-1} and 3670 cm^{-1} is assigned to {101} facet in the infrared region (Figure 3).[35] In addition, other facets such as {111} and {103} may explain the broadening of the band towards lower wavenumber values[8]. It is important to note, however, that the presence of the surfactant, particularly with a polar head, complicates the OH band by creating hydrogen bonds between the surfactant and surface O-H groups, making further study of the IR spectrum for this sample difficult.

All the rutile samples look like needles (Figure 4). The FFT analysis shows the {110} facet, as expected (Figure S4). [47] To get an idea of the possible facets present on the tips of the needles, some projected angles are given on the STEM-HAADF images (Figure 4). The value of the angle between the facets of the body and the tips is approximately 132°, which is consistent with the presence of {111} facets (Scheme 1) on the tips and {110} ones along the body. This is consistent with the typical morphology found in a previous study.[48]

We can observe that the 3725 cm^{-1} Ti-μ_1-OH band intensity increases with the length of the needle, i.e. the size of the {110} planes ($I_{R\text{-}Small} < I_{R\text{-}Mid} < I_{R\text{-}Long}$) (Figure 4). We can therefore assume that these Ti-μ_1-OH groups are preferentially located on the {110} facets of the nanoparticles.

A comparative analysis with Kipreos *et al*'s.[42] study of the O-H bands in rutile nanoparticles by DRIFT analysis (Table 2) reveals an additional low-intensity band observed around 3635 cm^{-1} in the R-Long and R-Mid samples (Figure 4). Moreover, the R-Small sample, which is the sample with the smallest dimensions, displays a shoulder at 3657 cm^{-1}. Given the facets of the tips are exacerbated in this sample (Table 1), we could hypothesize that the 3630-3640 cm^{-1} band corresponds to {110} facets while the 3657 cm^{-1} band corresponds to {111} facets in the case of bridging hydroxyls (bands due to Ti_V-μ_2-OH, see Table 2). Furthermore, the broadened band observed at 3675 cm^{-1} in the R-Small sample could be attributed to Ti_{IV}-μ_1-OH, potentially resulting from the deformation of the quadratic cell, as discussed in section 1.1. This μ_1-OH deformation could lead to the presence of a greater number of defects on the surface of the nanoparticle, and therefore justify a higher intensity for this band. Similarly, the band around 3700 cm^{-1} could be attributed to another Ti_{IV}-μ_1-OH site or facet.

The different band assignments of the O-H stretching band in bare titania nanoparticles are summarized in Table S2 of the SI.

In conclusion, even if anatase particles exhibit various morphologies, the observed stretching modes of the surface O-H bonds are all Ti-μ_1-OH or $-OH_2$ mainly onto {101} facets. The rutile nanoparticles predominantly exhibit a needle-like morphology that differs in size and, consequently, in the ratio of {111} and/or {101} tips compared to {110} lateral facets. The observed stretching modes of the surface O-H bonds are Ti-μ_2-OH mainly onto {111} and/or {101} tips, and Ti-μ_1-OH and μ_2-OH onto {110} lateral facets.

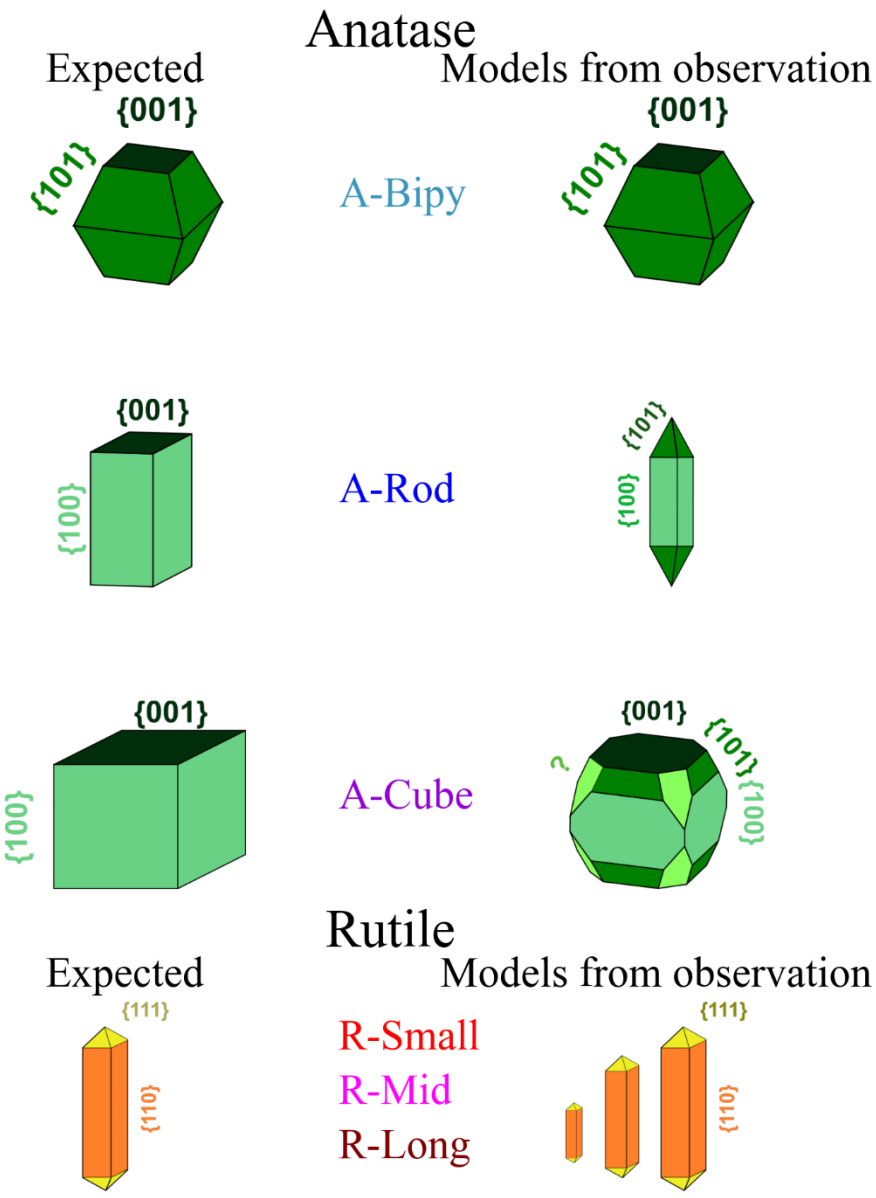

Scheme 1. *Expected morphologies for TiO_2 nanoparticles (left) compared with the facets observed using STEM-HAADF/iDPC, XRD and DRIFT analyses.*

1.5. Zeta potential measurements

Zeta potential values as a function of pH are shown in Figure 5 for the various samples. The isoelectric point (IEP) values for each sample are given in Table 1. In the literature, samples with anatase and rutile structures have similar isoelectric point values (around 6), as in our case (Figure 5).[49] However, in literature data, various synthesis conditions are used, and particle size and morphology are not discussed, making a detailed discussion of the effect of these parameters difficult.

The Smoluchowski approximation used for zeta potential calculations based on electrophoretic measurements considers spherical nanoparticles. Consequently, true morphologies are not taken into account. In the case of A-Bipy and A-Cube, the anisotropy ratio is close to 1, corresponding to quasi-spherical particles (Table 1). The value of the zeta potential is therefore well estimated. However, the lower IEP value (5.5) for the anatase cubes can be due to residual surfactant on the nanoparticles surface. In fact, oleic acid has a pKa close to 5, leading to a lower value for the isoelectric point.

In the case of R-Mid and R-Long, the anisotropy ratio is high (Table 1). Consequently, there is a greater error in estimating the zeta potential value from the measured electrophoretic mobility, whatever the pH value.

Finally, for all particles, at pH 2, zeta potential values are largely positive and close (Figure 5). Interaction with phosphate species, and in particular the dihydrogen phosphate anion ($H_2PO_4^-$), is therefore optimized under these conditions.

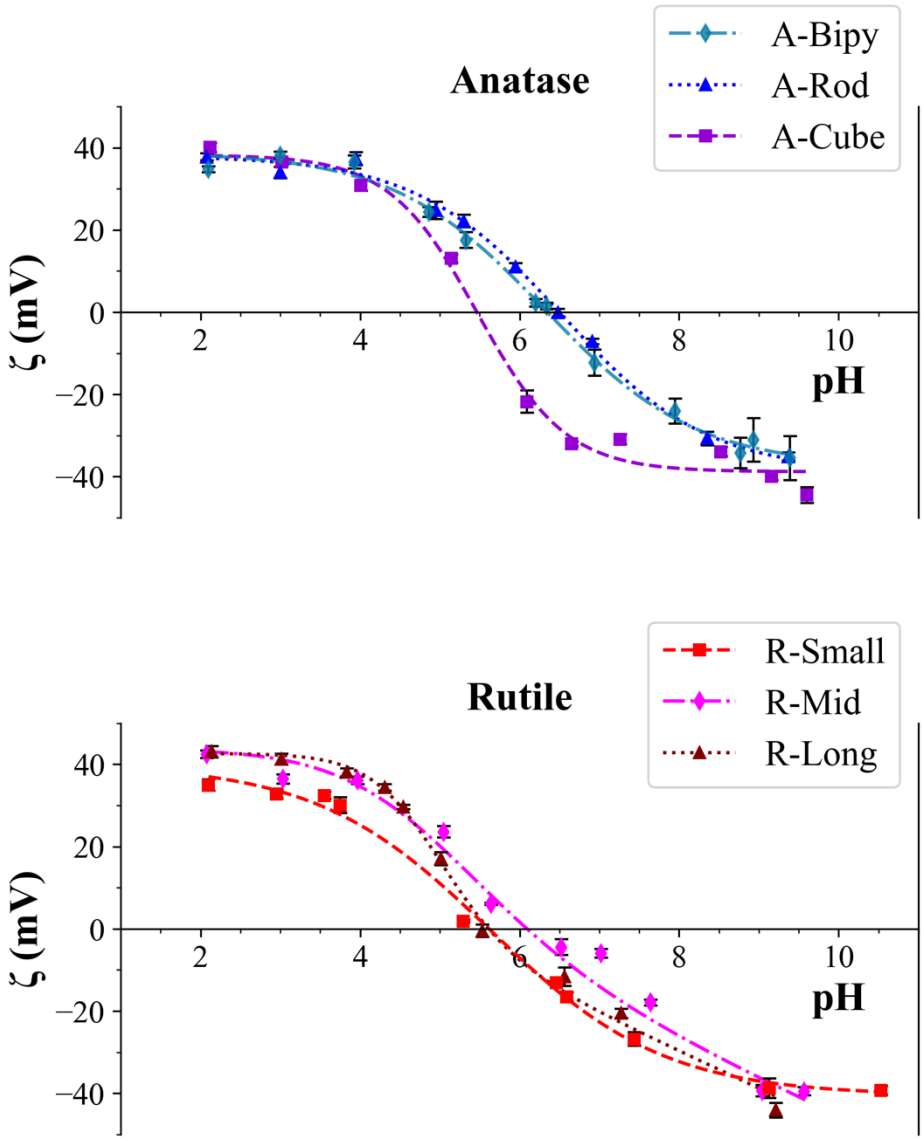

Figure 5. *Zeta potential measurements for the various TiO_2 nanoparticles. The lines are a guide for the eyes, while the points correspond to the experimental data.*

2. Phosphate species adsorption on TiO_2 nanoparticles

As discussed in the Materials and Methods part, our experimental work focused on a pH of 2, promoting the dihydrogen phosphate adsorption onto the particles, although H_3PO_4, which is present at a similar concentration, can also be adsorbed.[25,31,50,51]

2.1. Phosphate species adsorption isotherms

The adsorption isotherm curves shown in Figure 6 depict the adsorption behaviors of anatase and rutile. For a better comparison between experiments, phosphate species amounts are normalized per nm^2. Whatever the crystallographic nature and morphology, the maximum adsorption amount for phosphate species is 1.5 nm^{-2}, except for A-Cube and R-Mid samples. In the first case, the A-Cube sample has a lower phosphate coverage (1.2 phosphate species.nm^{-2}) potentially due to surfactants on the nanoparticles surface, preventing adsorption. R-Mid samples show a higher phosphate coverage (2.0 phosphate species.nm^{-2}), which, as discussed above, may be attributed to the needles aggregation, leading to a specific surface underestimation, and consequently, a higher adsorption amount per surface unit. The values obtained here are consistent with those of Guiot *et al*[25] who reported a similar value of 1.2 phosphate species.nm^{-2} at pH 2 for commercial anatase PC100. Of course, in all the phosphate adsorption experimental protocols available in the literature, the question of reproducibility arises. This is why the method used here to perform these isotherms is described in detail in the SI.

Even if there are no differences on a macroscopic scale (adsorption isotherms), there may be some on a microscopic scale, in terms of adsorption on the different facets. In fact, these local differences, if they exist, have little impact on the values measured macroscopically. Indeed, in the case of rutile nanoparticles, a zero-adsorption on the tips would only represent approximately a 0.1 phosphate species per nm^2 difference in the results. Furthermore, the anatase facet {101} has the same amount of Ti or O sites and a calculated surface energy quite similar to that of the rutile facet {110}.[52] In order to better understand the differences that may exist at the microscopic level between the different samples, infrared spectroscopy experiments were carried out for different levels of phosphate species adsorption.

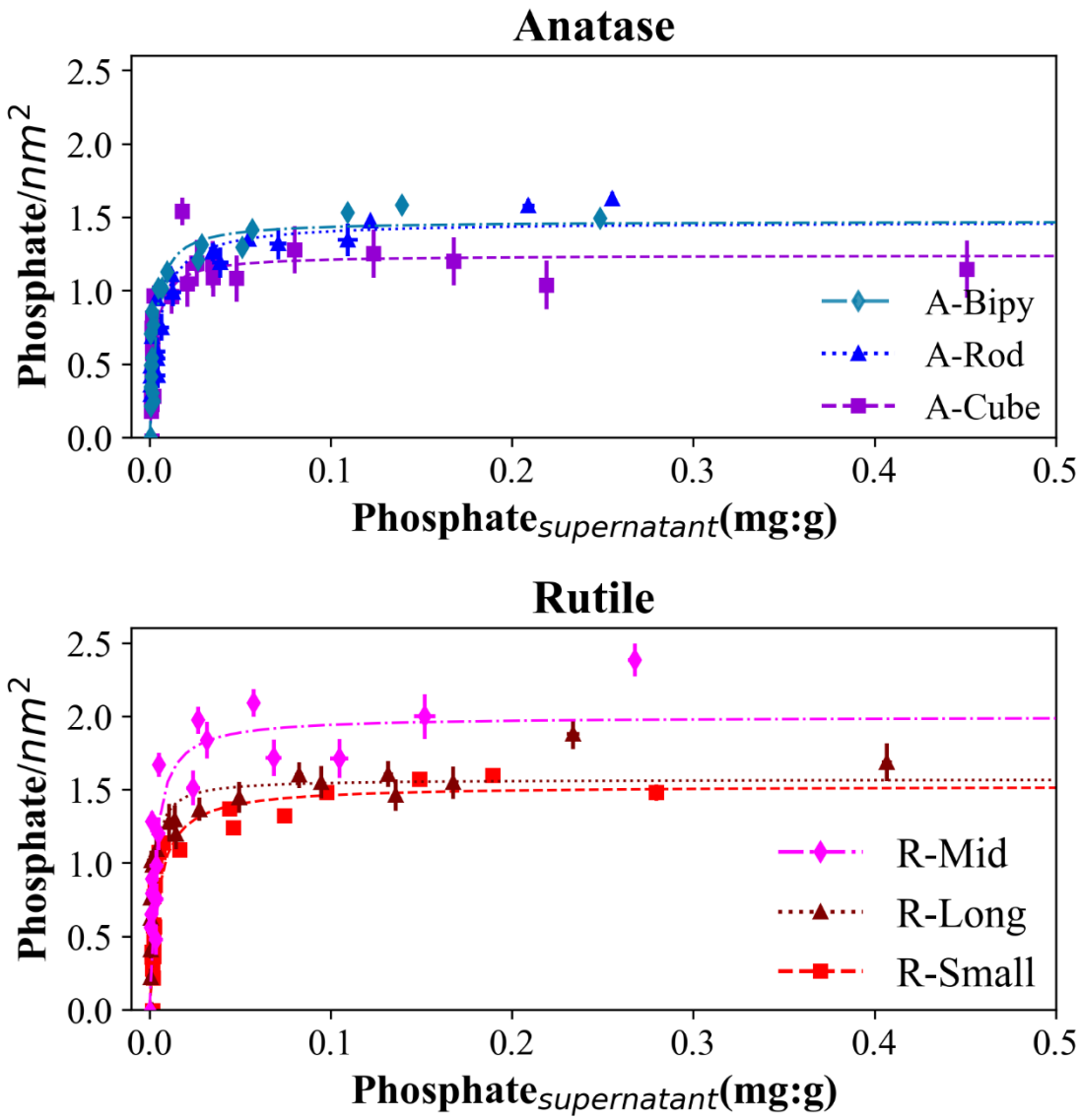

Figure 6. *Phosphate species adsorption isotherms on TiO_2 nanoparticles. Results are expressed as amount of phosphate species per nm^2. Lines correspond to curve fitting using the Langmuir model. The x-axis corresponds to the mass of phosphate species relative to the mass of supernatant.*

2.2. Phosphate species adsorption modes studied by infrared spectroscopy

The literature on adsorption of phosphate species on TiO_2 surfaces is relatively scarce, in contrast to the adsorption of phosphate species on various minerals, which has been the subject of simulations[53,54] or experiments[55], as illustrated by the case of the goethite mineral (α-FeOOH)[51,56–59] As described on Scheme 2, $H_2PO_4^-$ (the species we will be focusing on in the rest of the text) adsorption can be monodentate or bidentate with various modes (bridging

between two Ti^{4+}, or chelating to a single Ti^{4+}). Tridentate adsorption is less favorable, and is therefore not considered here.[25]

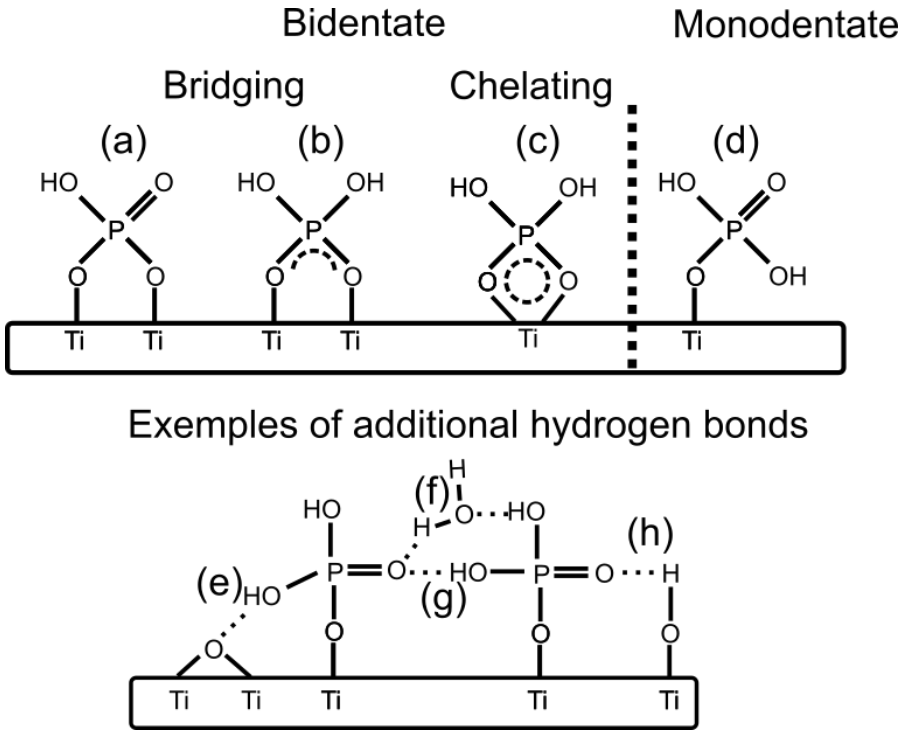

Scheme 2. *Representation of dihydrogenophosphate adsorption geometry on TiO_2 surface. Adsorption to the surface of titanium dioxide takes place via Ti-O-P bonds. (a-c) correspond to bidentate adsorption ((a-b): bridging and (c): chelating) whereas (d) is monodentate adsorption. (e-h) illustrate different types of H-bonds between various groups present on the TiO_2 surface.*

In what follows, we will use infrared spectroscopy in various spectral ranges to gain a better understanding of phosphate species adsorption on the different TiO_2 samples. The presence of phosphate species on the particles surface is confirmed by infrared spectroscopy (see below). As the powders are subjected to a flow of dry air, in order to dehydrate them as much as possible, we can assume that the species observed on the infrared spectra are mostly chemisorbed, as illustrated on Scheme 2, and that few physisorbed species remain on the surfaces. We investigated varying amounts of phosphate species on the nanoparticle's surfaces: low, medium or high (with the latter corresponding to the maximum value measured on the isotherm, see Figure 6).

P-O stretching modes between 950 and 1200 cm^{-1}

The P-O stretching modes in the 950-1200 cm^{-1} spectral region is influenced by factors such as the protonation state of the samples, the bidentate (chelating or non-chelating) or monodentate adsorption, the nature of the facet[51,56].

In this spectral range, FT-IR analyses were conducted using pellets made from dried titanium dioxide powders that had adsorbed various amounts of dihydrogen phosphate anions and diluted in KBr. In this range, all IR spectra for anatase samples appeared very similar. Similarly, rutile spectra presented bands with the same shape. We thus present here only the evolution of the signal, as a function of phosphate content for A-Bipy and R-long (Figure 7), and provide the other analyses in Figures S6 and S7.

Undoubtedly, the shape of the band, even with low absorbance, is mainly affected by the crystallographic nature of the sample, whether anatase or rutile. Anatase samples all exhibit a broad, nearly flat signal between 1000 and 1200 cm^{-1}. This signal presents two main bands: one at 1030 cm^{-1} and the other at around 1120 cm^{-1} (Figure 7a and S6). In the case of rutile, both components are present, but the spectrum is essentially centered on the one at around 1020-1040 cm^{-1}, with a shoulder around 1070 cm^{-1} (Figure 7b and S7).

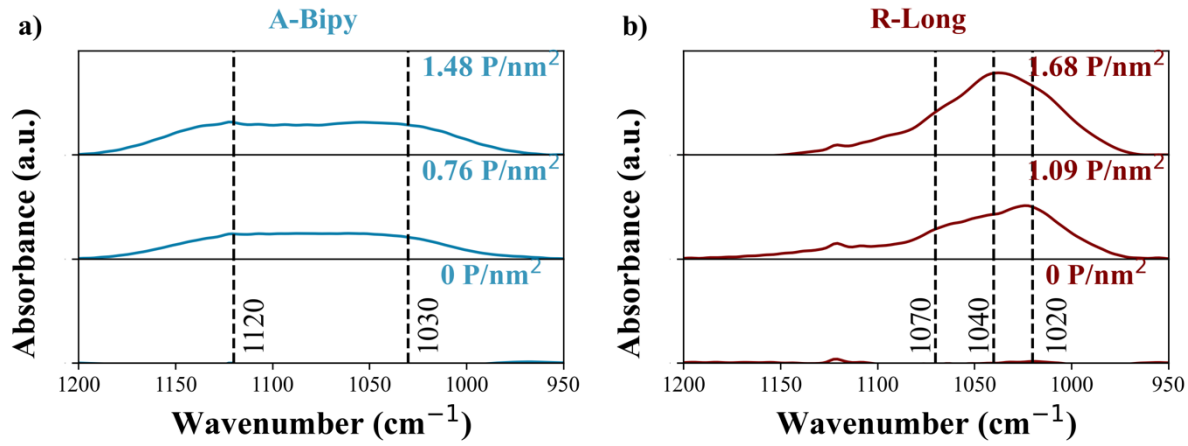

***Figure 7**. a) anatase (A-Bipy sample) and b) rutile (R-Long sample) infrared spectra in the 950-1200 cm^{-1} spectral region measured from KBr pellets for different points of the adsorption isotherm of $H_2PO_4^-$. Baseline has been subtracted. The dotted lines refer to some of the wavenumbers mentioned in the text.*

O-H stretching modes in the 3550-3750 cm^{-1} spectral region

The spectra measured in this spectral region are displayed in Figure 8, for all samples at various levels of phosphate species content (from the black to the lightest colors as the amount of phosphate species increases). As seen in Figure 3 and Table 2, bands between 3720 and 3740 cm^{-1} correspond to Ti_V-μ_1-OH on bare titania. These bands, when present, show low reactivity, as they are still present on the surface of the nanoparticles, even at the maximum phosphate coverage.

Upon phosphate adsorption, a new band appears at 3670 cm^{-1} for all samples. This band is assigned to the PO-H stretching mode,[60] confirming once again the presence of phosphate species onto the titania surface. As the amount of phosphate on the surface increases, the band shifts to lower wavenumbers. Note that a second band, with unclear attribution, appears around 3655 cm^{-1} as a more or less pronounced shoulder.

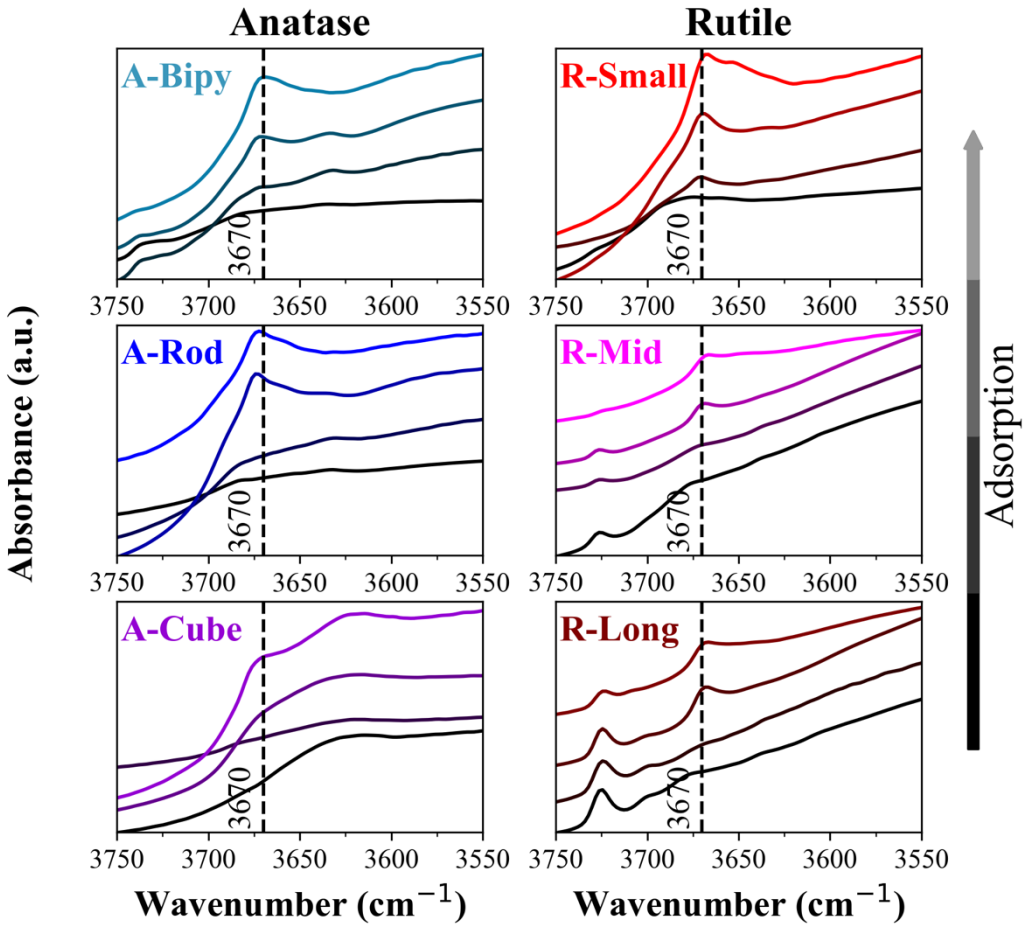

Figure 8. *Details of the infrared band corresponding to the O-H stretching mode for samples containing increasing amounts of adsorbed phosphate species. On each figure, bottom: no phosphate; top: higher levels of adsorbed phosphate species up to the maximum possible. All spectra were recorded after dehydration under dry air flow.*

Combination of stretching modes in the near infrared spectral range around 4650 cm^{-1}

Among the various modes of interest in the infrared spectral range, the modes of the POH group in the NIR range have attracted our attention. Few studies deal with this spectral region and generally focus on phosphate minerals.[61–64] Ishikawa *et al.* attribute the band around 4660 cm^{-1} to the combination of stretching modes ($\nu_{P\text{-}O}+\nu_{O\text{-}H}$) of P-O-H.[61] Here, it is the signature of adsorbed phosphate species having a PO-H group on the TiO_2 surface. In addition, Guiot *et al.* observed two bands at 4663 cm^{-1} and 4574 cm^{-1} still attributed to the combination of P-O and O-H stretching modes, as bidentate and monodentate, respectively.[25] Figure 9 presents experimental spectra of samples adsorbing increasing amounts of phosphate species. All bands were fitted with Gaussian curves (Figures S8-S10 and Table S3).

Upon phosphate adsorption, all samples present three new bands, more or less pronounced, around 4660 cm^{-1},, 4620 $cm^{-1}$and 4580 cm^{-1}.(Table S3). The position of these bands varies slightly between the different samples (see Table S3). Similar to the O-H bond stretching modes, the band maxima (around 4660 cm^{-1}) shift slightly towards lower wavenumbers with increasing phosphates adsorption on the surface (see also Table S3). Looking at the Gaussian decomposition of the spectra when the adsorption of phosphate species is maximal, we observe that the distribution of the three Gaussians is very similar, whatever the sample (Figure S10 and Table S3). Only the A-Cube sample exhibits a different behavior, with a greater contribution around 4620 cm^{-1} than for the other samples. This may be due to the presence of surfactants in this sample. For intermediate and maximum phosphate coverages, the spectra of the anatase and rutile samples are globally similar, except for the A-Cube sample (Figures S9 and S10).

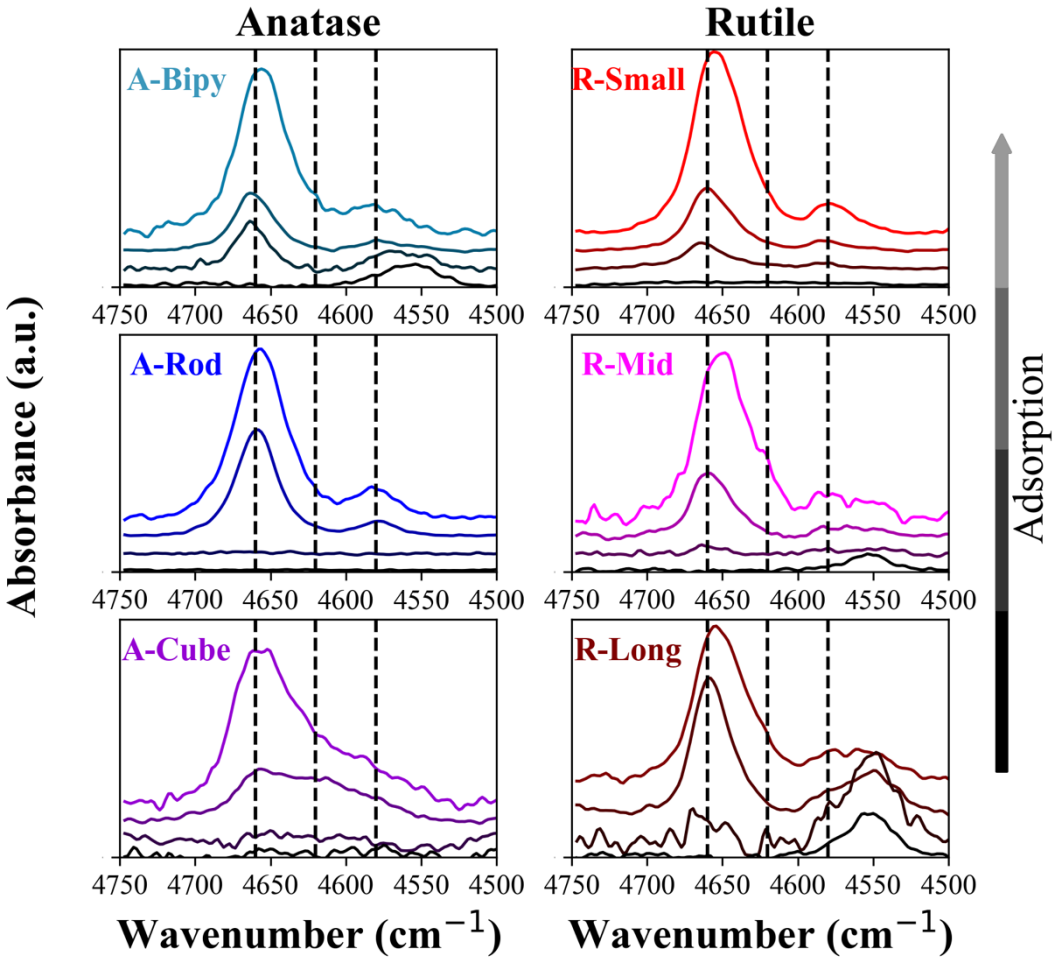

Figure 9. *Details of the infrared band corresponding to the combination of P-O-H stretching modes ($\nu_{P-O}+\nu_{O-H}$) for all samples containing: no phosphate, low, intermediate and maximum levels of phosphate species, respectively. Bottom (black): no phosphate, top (lightest color):*

higher levels of adsorbed phosphate species (maximum possible). All spectra were recorded after dehydration under dry air flow. All spectra are baseline corrected and shifted in (y) for clarity. In the case of A-Bipy, R-Mid and R-Long, samples without phosphate present an absorption around 4550 cm^{-1} whose origin is not clear. Dotted lines correspond to different components highlighted in the text (4580, 4620 and 4660 cm^{-1}).

2.3. Discussion

We propose to start our discussion with the evolution of the O-H stretching band (Figure 8). μ_1-OH and -OH_2 stretching band have been linked with the {101}, {100} and {110} anatase facets. Similarly, for rutile, μ_1-OH and μ_2-OH are on the {110} lateral facet whereas μ_2-OH stands on {111} and/or {101} tips. If we focus on rutile, R-Long present the largest {110} facet on which OH is adsorbed. Figure 8 clearly shows that the 3720-3740 cm^{-1} band's intensities (assigned to Ti_V-μ_1-OH) decrease with the adsorption of phosphate species. In the meantime, the intensity of the 3670 cm^{-1} band (assigned to PO-H stretching, see Figure 8) increases. This is the signature of phosphate species, replacing –OH groups on the surface of the nanoparticles. We observe the same trend, to a greater or lesser extent, for all the other samples.

For the remaining μ_1-OH, the band is slightly shifted, suggesting they remain partially isolated on the surface, without hydrogen bond interaction. On the other hand, the phosphate species band shifts towards lower values. Indeed, chemisorbed phosphate groups can interact (hydrogen-bond interactions) with other chemisorbed phosphate groups (Scheme 2)[65] or with remaining water molecules. The more phosphates are adsorbed, the closer they are to each other, leading to stronger H-bonds. Simulations showed that, on the {110} rutile facet, there were around 5 $Ti.nm^{-2}$.[52] With a phosphate coverage of 1.5 $phosphate.nm^{-2}$ and assuming bridging bidentate coordination (see next paragraph), 3 $Ti.nm^{-2}$ form Ti-O-P bonds, effectively leaving free -OH groups on the surface. In the case of rutile, another band can be followed: this is the band around 3680 cm^{-1} (Table 2) involving unsaturated titanium atoms. This band disappears completely as the phosphate coverage increases, suggesting higher reactivity compared to Ti-μ_1-OH sites. In the case of anatase samples, similar arguments can be made. All these data suggest strong surface heterogeneity after adsorption of phosphate species.

Some studies, whether experimental or using simulations, have looked at the adsorption of phosphorus-containing species (phosphate molecules, phosphonic acid[53,54]....) onto TiO_2 surfaces. The question on bidentate vs monodentate adsorption is thoughtfully discussed and debated. For example, Tielens *et al.* studied $H_2PO_4^-$ adsorption and determined that the most stable configuration for the {101} and {100} facets of anatase is bidentate[66] suggesting a

predominantly bidentate adsorption for phosphate on TiO_2 anatase.[67,68] In order to better understand the adsorption mode, we can dig further into the P-OH stretching mode, studied in the 950 – 1200 cm^{-1} spectral region (Figure 7 and Figures S6- S8). Literature stands that for goethite, the P-OH stretching mode bands between 800 and 1200 cm^{-1} are dependent on the state of protonation, facets and geometry of the adsorbed phosphate.[51,56–59] Indeed, the different groups attached to the phosphorus atom strongly influence the electron density around it and, therefore, the position of the bands.[69] In our case, as the band in the 950-1200 cm^{-1} spectral range has a low absorbance, it is not easy to distinguish the different bands observed in this spectral range and to attribute them to a given phosphate adsorbed species. We decided to discuss the evolution of the main components qualitatively. We have already established that in this domain, structure was more influent than morphology on the shape of the spectra. This mean that we can discuss all anatase and then rutile samples together.

In anatase samples, two components were distinguished: one around 1115 cm^{-1} and the other one at 1030 cm^{-1} (note that the component around 1122 cm^{-1}, present in all the spectra, is an artefact, see Table 3 for proposed assignments of the bands). Both bands increase with the phosphate coverage. The band around 1115 cm^{-1} can be attributed to PO modes in a bidentate adsorption coordination onto the surface.[25,51,58] More precise identification of this bidentate species is a matter of debate in the literature: initial studies suggest bridging adsorption,[58] while others identify it as chelating (Scheme 2).[25,51] The band around 1030 cm^{-1} is also attributed to a bidentate adsorption mode.[25,58] Although it is challenging to provide more precise details, these results are in agreement with a preferred bidentate adsorption on the facets of the anatase nanoparticles. Notably, in the case of the A-Cube sample, a less intense additional signal is observed between 1000 cm^{-1} and 950 cm^{-1}. This signal may be due to CH wag from the substituted alkene group in the surfactant (oleate), accounting for the wide bandwidth in this case.

Table 3. *Proposed assignments of the infrared bands detected around 1000 and 3600 cm^{-1} according to the sample type and the nature of the facet in the titania nanoparticles upon phosphate adsorption.*

♣ 950 – 1200 cm^{-1} spectral region (P-O mode)

Band	Anatase	Rutile
1030 cm^{-1} (1020-1040 cm^{-1})	Bidentate complex	Bidentate complex, mostly on {110} facet

1115 cm^{-1}	P-O in bidentate complex	P-O in bidentate complex, mostly on {110} facet
1070 cm^{-1} (shoulder), observed only at low phosphate rate		Monodentate complex on {111} facet

♣ 3550 – 3750 cm^{-1} spectral region (O-H stretching mode)

Band	Anatase	Rutile
3720-3740 cm^{-1}	Ti_V-μ_1-OH always present, even after adsorption	
3670 cm^{-1}	PO-H stretching mode	

In the case of rutile-type samples, the overall shape of the P-O stretching band differs from anatase (Figure 7, see also Table 3), but keeps similar components: a signal around 1115 cm^{-1}, which exhibits a weaker intensity, and one around 1030 cm^{-1}. As for anatase, the infrared spectra evolve with the amount of phosphate (Figure S7). At the start of adsorption, a band appears at 1020 cm^{-1}, together with a weak component around 1115 cm^{-1}. As the amount of phosphate increases, the components around 1030 cm^{-1} and 1040 cm^{-1} increase. As in the case of anatase samples, the components at 1030 cm^{-1} and 1115 cm^{-1} can be attributed to bidentate adsorption of phosphate species to the surface. Additionally, other components contribute to the overall appearance distinguishing it from that of anatase. In addition to bidentate adsorption, the presence of shoulders at 1070 cm^{-1} and 1020 cm^{-1} could be an indication of a different adsorption mode specific to rutile. In the case of rutile, {110} facets are more stable and abundant than {111} facets, which therefore possess higher energy.[70,71] Consequently, phosphate adsorption may be favored on the tips when the amount of phosphate is low, which explains why the band at 1070 cm^{-1} is visible very early in all three rutile samples. This is also consistent with the results of Hiji et al. [24] who show a slight kinetic and quantitative advantage of phosphate adsorption on the {111} single crystal over the {110} single crystal. As stated above, Ti-μ_1-OH groups are preferentially located on the {110} facets of the nanoparticles, and are not very reactive (Figure 8). They lead to phosphate species bidentate adsorption. On the

{111} facets of the rutile particles, there are mainly Ti_V-μ_2-OH. There are also very reactive Ti_{IV}-μ_1-OH sites on the {101} facets. On these {111} and/or {101} facets, a preferential monodentate phosphate adsorption occurs. The early appearance of a band at 1020 cm^{-1} in rutile samples, different from that of anatase, could also be an indication of monodentate adsorption, which could be favored by the reactivity of the {111} tips. The different assignments of the bands located around 1000 and 3600 cm^{-1} upon phosphate adsorption are summarized in Table 3.

Lastly, in the near-infrared range, the modes at 4660 and 4580 cm^{-1} (Figure 9) were previously attributed to the combination of stretching modes of P-O and O-H in dihydrogen phosphate species adsorbed bidentate and monodentate, respectively, on the surface.[25] However, all samples behave in the same way in this spectral range, whether anatase or rutile, raising questions about the attributions made. As the O-H stretching band at 3670 cm^{-1} does not differ greatly between the anatase and rutile samples, the P-O vibrational mode involved, between 1000 cm^{-1} and 1120 cm^{-1}, should not vary between the two phases. Otherwise, a difference would be observed in the bands detected around 4600 cm^{-1}. We can therefore assume that it is the P-O band located around 1030-1040 cm^{-1} in anatase and rutile that is involved in the combination mode, corresponding to a more constrained bidentate adsorption, and not the others.

CONCLUSION

In this study, we investigated the adsorption behavior of phosphate species on various nanoparticle crystalline structures (anatase and rutile). To this end, different nanoparticle geometries were synthesized, and their crystalline facets were characterized by different techniques such as XRD, and STEM-HAADF. Anatase samples exhibited more varied geometries, including bipyramids, needles, cubes, while rutile systematically formed needles with various aspect ratios. For the latter, it was possible to vary the amount of {111} facets present at the lower and upper edges of the needles, in comparison to {110} facets along the height of the needles.

The zeta potential measurements showed IEP values close to the expected ones for TiO_2 particles (around 6). Phosphate species adsorption experiments were then carried out at pH 2 to maximize adsorption. Overall, at saturation, nanoparticle surfaces were covered with a

phosphate amount of 1.5 phosphate.nm^{-2}. This value is independent of geometry and crystalline phase.

To gain insights into the microscopic view of the adsorption process, infrared spectroscopy experiments were carried out on various samples, which had adsorbed (or not) varying amounts of phosphate species and had been dried. Spectral ranges from near-infrared to mid-infrared were investigated to provide a comprehensive view of the adsorption phenomena. Results showed that the adsorption of phosphate species does not occur randomly on nanoparticle facets. Indeed, crystal phase and facet type influence the nature of this adsorption. Specifically, adsorption is preferably bidentate (bridging or chelating), depending on the facets of anatase-type samples, whereas it is probably monodentate on the {111} and/or {101} tips of rutile-type samples, with bidentate adsorption on the lateral {110} facets.

Finally, the study revealed that not all OH groups on bare nanoparticle surfaces exhibit equal reactivity towards phosphate species. The Ti_V-μ_1-OH groups showed low reactivity, leading to a coexistence of phosphate species and -OH groups on the surfaces, even at the maximum phosphate coverage.

These results highlight the significance of crystal structure and the nature of the exposed facets in determining the adsorption mode of phosphate anions on TiO_2 nanoparticles. Further investigations into the evolution of these adsorption processes under different parameters such as solution pH, for example, in order to approach a physiological pH, could provide additional valuable insights.

ASSOCIATED CONTENT

Supporting Information

Synthesis of the nanoparticles, distribution of the particle size in length and width, DRIFT spectra of the TiO_2 nanoparticles, Fast Fourier Transform of images (Figure 4 in the main text), image of nanoparticles aggregation on TEM grid, O-H stretching band assignments, phosphate species isotherms measurement and construction, infrared bands in the 940-1250 cm^{-1} spectral region, simulation of combination modes (P-O and O-H) in the NIR spectral region for different levels of surface adsorption

NOTE

The authors declare no competing financial interest.

ACKNOWLEDGMENTS

Funding from the Agence Nationale de la Recherche (ANR ACETONE N° ANR-20-CE09-0010-01) is gratefully acknowledged. The authors want to thank Patrick Le Griel and Eric Gautron for the TEM experiments, Mohamed Selmane for the XRD experiments and Charles Rivron for the BET measurements.

REFERENCES

(1) *Home | Nanotechnology Products Database | NPD*. https://product.statnano.com// (accessed 2023-05-22).

(2) Baranowska-Wójcik, E.; Szwajgier, D.; Oleszczuk, P.; Winiarska-Mieczan, A. Effects of Titanium Dioxide Nanoparticles Exposure on Human Health—a Review. *Biol. Trace Elem. Res.* **2020**, *193* (1), 118–129. https://doi.org/10.1007/s12011-019-01706-6.

(3) Fujishima, A.; Zhang, X.; Tryk, D. TiO2 Photocatalysis and Related Surface Phenomena. *Surf. Sci. Rep.* **2008**, *63* (12), 515–582. https://doi.org/10.1016/j.surfrep.2008.10.001.

(4) Cassaignon, S.; Colbeau-Justin, C.; Durupthy, O. Titanium Dioxide in Photocatalysis. In *Nanomaterials: A Danger or a Promise?*; Brayner, R., Fiévet, F., Coradin, T., Eds.; Springer London: London, 2013; pp 153–188. https://doi.org/10.1007/978-1-4471-4213-3_6.

(5) Linsebigler, A. L.; Lu, G.; Yates, J. T. Photocatalysis on TiO2 Surfaces: Principles, Mechanisms, and Selected Results. *Chem. Rev.* **1995**, *95* (3), 735–758. https://doi.org/10.1021/cr00035a013.

(6) Pigeot-Rémy, S.; Gregori, D.; Hazime, R.; Hérissan, A.; Guillard, C.; Ferronato, C.; Cassaignon, S.; Colbeau-Justin, C.; Durupthy, O. Size and Shape Effect on the Photocatalytic Efficiency of TiO_2 Brookite. *J. Mater. Sci.* **2019**, *54* (2), 1213–1225. https://doi.org/10.1007/s10853-018-2924-x.

(7) Pigeot-Rémy, S.; Dufour, F.; Herissan, A.; Ruaux, V.; Maugé, F.; Hazime, R.; Foronato, C.; Guillard, C.; Chaneac, C.; Durupthy, O.; Colbeau-Justin, C.; Cassaignon, S. Bipyramidal Anatase TiO_2 Nanoparticles, a Highly Efficient Photocatalyst? Towards a Better Understanding of the Reactivity. *Appl. Catal. B Environ.* **2017**, *203*, 324–334. https://doi.org/10.1016/j.apcatb.2016.10.031.

(8) Dufour, F.; Pigeot-Remy, S.; Durupthy, O.; Cassaignon, S.; Ruaux, V.; Torelli, S.; Mariey, L.; Maugé, F.; Chanéac, C. Morphological Control of TiO_2 Anatase Nanoparticles: What Is the Good Surface Property to Obtain Efficient Photocatalysts? *Appl. Catal. B Environ.* **2015**, *174–175*, 350–360. https://doi.org/10.1016/j.apcatb.2015.03.013.

(9) Magne, C.; Dufour, F.; Labat, F.; Lancel, G.; Durupthy, O.; Cassaignon, S.; Pauporté, Th. Effects of TiO_2 Nanoparticle Polymorphism on Dye-Sensitized Solar Cell Photovoltaic Properties. *J. Photochem. Photobiol. Chem.* **2012**, *232*, 22–31. https://doi.org/10.1016/j.jphotochem.2012.01.015.

(10) de la Calle, I.; Menta, M.; Klein, M.; Séby, F. Screening of TiO_2 and Au Nanoparticles in Cosmetics and Determination of Elemental Impurities by Multiple Techniques (DLS, SP-ICP-MS, ICP-MS and ICP-OES). *Talanta* **2017**, *171*, 291–306. https://doi.org/10.1016/j.talanta.2017.05.002.

(11) Taboada-López, M. V.; Herbello-Hermelo, P.; Domínguez-González, R.; Bermejo-Barrera, P.; Moreda-Piñeiro, A. Enzymatic Hydrolysis as a Sample Pre-Treatment for Titanium Dioxide Nanoparticles Assessment in Surimi (Crab Sticks) by Single Particle ICP-MS. *Talanta* **2019**, *195*, 23–32. https://doi.org/10.1016/j.talanta.2018.11.023.

(12) Dudefoi, W.; Terrisse, H.; Richard-Plouet, M.; Gautron, E.; Popa, F.; Humbert, B.; Ropers, M.-H. Criteria to Define a More Relevant Reference Sample of Titanium Dioxide in the Context of Food: A Multiscale Approach. *Food Addit. Contam. Part A* **2017**, 1–13. https://doi.org/10.1080/19440049.2017.1284346.

(13) Dudefoi, W.; Rabesona, H.; Rivard, C.; Mercier-Bonin, M.; Humbert, B.; Terrisse, H.; Ropers, M.-H. *In Vitro* Digestion of Food Grade TiO_2 (E171) and TiO_2 Nanoparticles: Physicochemical Characterization and Impact on the Activity of Digestive Enzymes. *Food Funct.* **2021**, *12* (13), 5975–5988. https://doi.org/10.1039/D1FO00499A.

(14) Ropers, M.-H.; Terrisse, H.; Mercier-Bonin, M.; Humbert, B. Titanium Dioxide as Food Additive. In *Application of Titanium Dioxide*; Janus, M., Ed.; InTech, 2017. https://doi.org/10.5772/intechopen.68883.

(15) Jovanović, B.; Jovanović, N.; Cvetković, V. J.; Matić, S.; Stanić, S.; Whitley, E. M.; Mitrović, T. Lj. The Effects of a Human Food Additive, Titanium Dioxide Nanoparticles E171, on Drosophila Melanogaster - a 20 Generation Dietary Exposure Experiment. *Sci. Rep.* **2018**, *8* (1), 17922. https://doi.org/10.1038/s41598-018-36174-w.

(16) Hong, F.; Yu, X.; Wu, N.; Zhang, Y.-Q. Progress of in Vivo Studies on the Systemic Toxicities Induced by Titanium Dioxide Nanoparticles. *Toxicol. Res.* **2017**, *6* (2), 115–133. https://doi.org/10.1039/C6TX00338A.

(17) Bettini, S.; Boutet-Robinet, E.; Cartier, C.; Coméra, C.; Gaultier, E.; Dupuy, J.; Naud, N.; Taché, S.; Grysan, P.; Reguer, S.; Thieriet, N.; Réfrégiers, M.; Thiaudière, D.; Cravedi, J.-P.; Carrière, M.; Audinot, J.-N.; Pierre, F. H.; Guzylack-Piriou, L.; Houdeau, E. Food-Grade TiO_2 Impairs Intestinal and Systemic Immune Homeostasis, Initiates Preneoplastic Lesions and Promotes Aberrant Crypt Development in the Rat Colon. *Sci. Rep.* **2017**, *7* (1), 40373. https://doi.org/10.1038/srep40373.

(18) *Arrêté Du 21 Décembre 2021 Portant Suspension de La Mise Sur Le Marché Des Denrées Contenant l'additif E 171 (Dioxyde de Titane - TiO2)*; 2021.

(19) Shi, H.; Magaye, R.; Castranova, V.; Zhao, J. Titanium Dioxide Nanoparticles: A Review of Current Toxicological Data. *Part. Fibre Toxicol.* **2013**, *10* (1), 15. https://doi.org/10.1186/1743-8977-10-15.

(20) EFSA Panel on Food Additives and Nutrient Sources added to Food (ANS). Re-evaluation of Titanium Dioxide (E 171) as a Food Additive. *EFSA J.* **2016**, *14* (9). https://doi.org/10.2903/j.efsa.2016.4545.

(21) Musial, J.; Krakowiak, R.; Mlynarczyk, D. T.; Goslinski, T.; Stanisz, B. J. Titanium Dioxide Nanoparticles in Food and Personal Care Products—What Do We Know about Their Safety? *Nanomaterials* **2020**, *10* (6), 1110. https://doi.org/10.3390/nano10061110.

(22) Hou, J.; Wang, L.; Wang, C.; Zhang, S.; Liu, H.; Li, S.; Wang, X. Toxicity and Mechanisms of Action of Titanium Dioxide Nanoparticles in Living Organisms. *J. Environ. Sci.* **2019**, *75*, 40–53. https://doi.org/10.1016/j.jes.2018.06.010.

(23) Le, Q.-C.; Ropers, M.-H.; Terrisse, H.; Humbert, B. Interactions between Phospholipids and Titanium Dioxide Particles. *Colloids Surf. B Biointerfaces* **2014**, *123*, 150–157. https://doi.org/10.1016/j.colsurfb.2014.09.010.

(24) Hiji, A.; Hanawa, T.; Yokoi, T.; Chen, P.; Ashida, M.; Kawashita, M. Time Transient of Calcium and Phosphate Ion Adsorption by Rutile Crystal Facets in Hanks' Solution Characterized by XPS. *Langmuir* **2021**, *37* (12), 3597–3604. https://doi.org/10.1021/acs.langmuir.0c03540.

(25) Guiot, F.; Praud, C.; Quillard, S.; Humbert, B.; Ropers, M.-H.; Paris, M.; Terrisse, H. Surface Reactivity of Anatase Particles towards Phosphated Species. *Colloids Surf. Physicochem. Eng. Asp.* **2022**, *655*, 130232. https://doi.org/10.1016/j.colsurfa.2022.130232.

(26) Sugimoto, T.; Zhou, X.; Muramatsu, A. Synthesis of Uniform Anatase TiO_2 Nanoparticles by Gel–Sol Method. *J. Colloid Interface Sci.* **2003**, *259* (1), 53–61. https://doi.org/10.1016/S0021-9797(03)00035-3.

(27) Pottier, A.; Cassaignon, S.; Chanéac, C.; Villain, F.; Tronc, E.; Jolivet, J.-P. Size Tailoring of TiO_2 Anatase Nanoparticles in Aqueous Medium and Synthesis of Nanocomposites. Characterization by Raman Spectroscopy. *J. Mater. Chem.* **2003**, *13* (4), 877–882. https://doi.org/10.1039/b211271j.

(28) Pottier, A.; Chanéac, C.; Tronc, E.; Mazerolles, L.; Jolivet, J.-P. Synthesis of Brookite TiO_2 Nanoparticles by Thermolysis of $TiCl_4$ in Strongly Acidic Aqueous Media. *J. Mater. Chem.* **2001**, *11* (4), 1116–1121. https://doi.org/10.1039/b100435m.

(29) Cassaignon, S.; Koelsch, M.; Jolivet, J.-P. From TiCl3 to TiO2 Nanoparticles (Anatase, Brookite and Rutile): Thermohydrolysis and Oxidation in Aqueous Medium. *J. Phys. Chem. Solids* **2007**, *68* (5–6), 695–700. https://doi.org/10.1016/j.jpcs.2007.02.020.

(30) Dufour, F.; Cassaignon, S.; Durupthy, O.; Colbeau-Justin, C.; Chanéac, C. Do TiO $_2$ Nanoparticles Really Taste Better When Cooked in a Microwave Oven? *Eur. J. Inorg. Chem.* **2012**, *2012* (16), 2707–2715. https://doi.org/10.1002/ejic.201101269.

(31) Hühn, A.; Wisser, D.; Corral Valero, M.; Roy, T.; Rivallan, M.; Catita, L.; Lesage, A.; Michel, C.; Raybaud, P. Structural Characterization of Phosphate Species Adsorbed on γ-Alumina by Combining DNP Surface Enhanced NMR Spectroscopy and DFT Calculations. *ACS Catal.* **2021**, *11* (17), 11278–11292. https://doi.org/10.1021/acscatal.1c02135.

(32) Barrows, J. N.; Jameson, G. B.; Pope, M. T. Structure of a Heteropoly Blue. The Four-Electron Reduced .Beta.-12-Molybdophosphate Anion. *J. Am. Chem. Soc.* **1985**, *107* (6), 1771–1773. https://doi.org/10.1021/ja00292a059.

(33) Pelletier, M.; Michot, L. J.; Barres, O.; Humbert, B.; Petit, S.; Robert, J. L. Influence of KBr Conditioning on the Infrared Hydroxyl-Stretching Region of Saponites. *Clay Miner.* **1999**, *34* (3), 439–445.

(34) Rinnert, E.; Carteret, C.; Humbert, B.; Fragneto-Cusani, G.; Ramsay, J. D. F.; Delville, A.; Robert, J.-L.; Bihannic, I.; Pelletier, M.; Michot, L. J. Hydration of a Synthetic Clay with Tetrahedral Charges: A Multidisciplinary Experimental and Numerical Study. *J. Phys. Chem. B* **2005**, *109* (49), 23745–23759. https://doi.org/10.1021/jp050957u.

(35) Arrouvel, C.; Digne, M.; Breysse, M.; Toulhoat, H.; Raybaud, P. Effects of Morphology on Surface Hydroxyl Concentration: A DFT Comparison of Anatase–TiO_2 and γ-Alumina Catalytic Supports. *J. Catal.* **2004**, *222* (1), 152–166. https://doi.org/10.1016/j.jcat.2003.10.016.

(36) Dzwigaj, S.; Arrouvel, C.; Breysse, M.; Geantet, C.; Inoue, S.; Toulhoat, H.; Raybaud, P. DFT Makes the Morphologies of Anatase-TiO2 Nanoparticles Visible to IR Spectroscopy. *J. Catal.* **2005**, *236* (2), 245–250. https://doi.org/10.1016/j.jcat.2005.09.034.

(37) Busca, G.; Saussey, H.; Saur, O.; Lavalley, J. C.; Lorenzelli, V. FT-IR Characterization of the Surface Acidity of Different Titanium Dioxide Anatase Preparations. *Appl. Catal.* **1985**, *14*, 245–260. https://doi.org/10.1016/S0166-9834(00)84358-4.

(38) Morterra, C. An Infrared Spectroscopic Study of Anatase Properties. Part 6.—Surface Hydration and Strong Lewis Acidity of Pure and Sulphate-Doped Preparations. *J. Chem. Soc. Faraday Trans. 1 Phys. Chem. Condens. Phases* **1988**, *84* (5), 1617. https://doi.org/10.1039/f19888401617.

(39) Van Veen, J. A. R. An Enquiry into the Surface Chemistry of TiO_2 (Anatase). *Z. Für Phys. Chem.* **1989**, *162* (2), 215–229. https://doi.org/10.1524/zpch.1989.162.Part_2.215.

(40) Travert, A.; Manoilova, O. V.; Tsyganenko, A. A.; Maugé, F.; Lavalley, J. C. Effect of Hydrogen Sulfide and Methanethiol Adsorption on Acidic Properties of Metal Oxides: An Infrared Study. *J. Phys. Chem. B* **2002**, *106* (6), 1350–1362. https://doi.org/10.1021/jp0126762.

(41) Hadjiivanov, K. I.; Klissurski, D. G. Surface Chemistry of Titania (Anatase) and Titania-Supported Catalysts. *Chem. Soc. Rev.* **1996**, *25* (1), 61. https://doi.org/10.1039/cs9962500061.

(42) Kipreos, M. D.; Foster, M. Water Interactions on the Surface of 50 nm Rutile TiO_2 Nanoparticles Using in Situ DRIFTS. *Surf. Sci.* **2018**, *677*, 1–7. https://doi.org/10.1016/j.susc.2018.05.005.

(43) Deiana, C.; Fois, E.; Coluccia, S.; Martra, G. Surface Structure of TiO_2 P25 Nanoparticles: Infrared Study of Hydroxy Groups on Coordinative Defect Sites. *J. Phys. Chem. C* **2010**, *114* (49), 21531–21538. https://doi.org/10.1021/jp107671k.

(44) Minella, M.; Faga, M. G.; Maurino, V.; Minero, C.; Pelizzetti, E.; Coluccia, S.; Martra, G. Effect of Fluorination on the Surface Properties of Titania P25 Powder: An FTIR Study. *Langmuir* **2010**, *26* (4), 2521–2527. https://doi.org/10.1021/la902807g.

(45) Lazzeri, M.; Vittadini, A.; Selloni, A. Structure and Energetics of Stoichiometric TiO 2 Anatase Surfaces. *Phys. Rev. B* **2001**, *63* (15), 155409. https://doi.org/10.1103/PhysRevB.63.155409.

(46) Ali Ahmad, M.; Prelot, B.; Dufour, F.; Durupthy, O.; Razafitianamaharavo, A.; Douillard, J. M.; Chaneac, C.; Villiéras, F.; Zajac, J. Influence of Morphology and Crystallinity on Surface Reactivity of Nanosized Anatase TiO_2 Studied by Adsorption Techniques. 2. Solid–Liquid Interface. *J. Phys. Chem. C* **2013**, *117* (9), 4459–4469. https://doi.org/10.1021/jp3077084.

(47) Ramamoorthy, M.; Vanderbilt, D.; King-Smith, R. D. First-Principles Calculations of the Energetics of Stoichiometric TiO 2 Surfaces. *Phys. Rev. B* **1994**, *49* (23), 16721–16727. https://doi.org/10.1103/PhysRevB.49.16721.

(48) Koelsch, M. Nanoparticules de TiO_2 : Contrôle Structural, Morphologique, Dimensionnel et Propriétés Électrochimiques, 2004.

(49) Kosmulski, M. The Significance of the Difference in the Point of Zero Charge between Rutile and Anatase. *Adv. Colloid Interface Sci.* **2002**, *99* (3), 255–264. https://doi.org/10.1016/S0001-8686(02)00080-5.

(50) Kang, S. A.; Li, W.; Lee, H. E.; Phillips, B. L.; Lee, Y. J. Phosphate Uptake by TiO_2: Batch Studies and NMR Spectroscopic Evidence for Multisite Adsorption. *J. Colloid Interface Sci.* **2011**, *364* (2), 455–461. https://doi.org/10.1016/j.jcis.2011.07.088.

(51) Ahmed, A. A.; Gypser, S.; Leinweber, P.; Freese, D.; Kühn, O. Infrared Spectroscopic Characterization of Phosphate Binding at the Goethite–Water Interface. *Phys. Chem. Chem. Phys.* **2019**, *21* (8), 4421–4434. https://doi.org/10.1039/C8CP07168C.

(52) Panagiotou, G. D.; Petsi, T.; Bourikas, K.; Garoufalis, C. S.; Tsevis, A.; Spanos, N.; Kordulis, C.; Lycourghiotis, A. Mapping the Surface (Hydr)Oxo-Groups of Titanium Oxide

and Its Interface with an Aqueous Solution: The State of the Art and a New Approach. *Adv. Colloid Interface Sci.* **2008**, *142* (1–2), 20–42. https://doi.org/10.1016/j.cis.2008.04.003.

(53) Nilsing, M.; Lunell, S.; Persson, P.; Ojamäe, L. Phosphonic Acid Adsorption at the TiO_2 Anatase (101) Surface Investigated by Periodic Hybrid HF-DFT Computations. *Surf. Sci.* **2005**, *582* (1–3), 49–60. https://doi.org/10.1016/j.susc.2005.02.044.

(54) Luschtinetz, R.; Frenzel, J.; Milek, T.; Seifert, G. Adsorption of Phosphonic Acid at the TiO_2 Anatase (101) and Rutile (110) Surfaces. *J. Phys. Chem. C* **2009**, *113* (14), 5730–5740. https://doi.org/10.1021/jp8110343.

(55) Guerrero, G.; Mutin, P. H.; Vioux, A. Anchoring of Phosphonate and Phosphinate Coupling Molecules on Titania Particles. *Chem. Mater.* **2001**, *13* (11), 4367–4373. https://doi.org/10.1021/cm001253u.

(56) Kubicki, J. D.; Paul, K. W.; Kabalan, L.; Zhu, Q.; Mrozik, M. K.; Aryanpour, M.; Pierre-Louis, A.-M.; Strongin, D. R. ATR–FTIR and Density Functional Theory Study of the Structures, Energetics, and Vibrational Spectra of Phosphate Adsorbed onto Goethite. *Langmuir* **2012**, *28* (41), 14573–14587. https://doi.org/10.1021/la303111a.

(57) Weng, Y.; Vekeman, J.; Zhang, H.; Chou, L.; Elskens, M.; Tielens, F. Unravelling Phosphate Adsorption on Hydrous Ferric Oxide Surfaces at the Molecular Level. *Chemosphere* **2020**, *261*, 127776. https://doi.org/10.1016/j.chemosphere.2020.127776.

(58) Tejedor-Tejedor, M. I.; Anderson, M. A. The Protonation of Phosphate on the Surface of Goethite as Studied by CIR-FTIR and Electrophoretic Mobility. *Langmuir* **1990**, *6* (3), 602–611. https://doi.org/10.1021/la00093a015.

(59) Persson, P.; Nilsson, N.; Sjöberg, S. Structure and Bonding of Orthophosphate Ions at the Iron Oxide–Aqueous Interface. *J. Colloid Interface Sci.* **1996**, *177* (1), 263–275. https://doi.org/10.1006/jcis.1996.0030.

(60) Low, M. J. D.; Ramamurthy, P. Infrared Study of the Surface Properties of Phosphoric Acid Impregnated Silica. *J. Phys. Chem.* **1968**, *72* (9), 3161–3167. https://doi.org/10.1021/j100855a014.

(61) Ishikawa, T.; Wakamura, M.; Kondo, S. Surface Characterization of Calcium Hydroxylapatite by Fourier Transform Infrared Spectroscopy. *Langmuir* **1989**, *5* (1), 140–144. https://doi.org/10.1021/la00085a025.

(62) Reddy, B. J.; Frost, R. L.; Palmer, S. J. A Near-Infrared Spectroscopic Study of the Phosphate Mineral Pyromorphite $Pb_5(PO_4)_3Cl$. *Spectrochim. Acta. A. Mol. Biomol. Spectrosc.* **2008**, *71* (2), 430–435. https://doi.org/10.1016/j.saa.2007.12.030.

(63) Campos, P. V.; Albuquerque, A. R. L.; Angélica, R. S.; Paz, S. P. A. FTIR Spectral Signatures of Amazon Inorganic Phosphates: Igneous, Weathering, and Biogenetic Origin. *Spectrochim. Acta. A. Mol. Biomol. Spectrosc.* **2021**, *251*, 119476. https://doi.org/10.1016/j.saa.2021.119476.

(64) Kolmas, J.; Marek, D.; Kolodziejski, W. Near-Infrared (NIR) Spectroscopy of Synthetic Hydroxyapatites and Human Dental Tissues. *Appl. Spectrosc.* **2015**, *69* (8), 902–912. https://doi.org/10.1366/14-07720.

(65) Brodard-Severac, F.; Guerrero, G.; Maquet, J.; Florian, P.; Gervais, C.; Mutin, P. H. High-Field ^{17}O MAS NMR Investigation of Phosphonic Acid Monolayers on Titania. *Chem. Mater.* **2008**, *20* (16), 5191–5196. https://doi.org/10.1021/cm8012683.

(66) Tielens, F.; Gervais, C.; Deroy, G.; Jaber, M.; Stievano, L.; Coelho Diogo, C.; Lambert, J.-F. Characterization of Phosphate Species on Hydrated Anatase TiO_2 Surfaces. *Langmuir* **2016**, *32* (4), 997–1008. https://doi.org/10.1021/acs.langmuir.5b03519.

(67) Connor, P. A.; McQuillan, A. J. Phosphate Adsorption onto TiO_2 from Aqueous Solutions: An in Situ Internal Reflection Infrared Spectroscopic Study. *Langmuir* **1999**, *15* (8), 2916–2921. https://doi.org/10.1021/la980894p.

(68) Gong, W. A Real Time in Situ ATR-FTIR Spectroscopic Study of Linear Phosphate Adsorption on Titania Surfaces. *Int. J. Miner. Process.* **2001**, *63* (3), 147–165. https://doi.org/10.1016/S0301-7516(01)00045-X.

(69) Daou, T. J.; Begin-Colin, S.; Grenèche, J. M.; Thomas, F.; Derory, A.; Bernhardt, P.; Legaré, P.; Pourroy, G. Phosphate Adsorption Properties of Magnetite-Based Nanoparticles. *Chem. Mater.* **2007**, *19* (18), 4494–4505. https://doi.org/10.1021/cm071046v.

(70) Oliver, P. M.; Watson, G. W.; Kelsey, E. T.; Parker, S. C. Atomistic Simulation of the Surface Structure of the TiO_2 Polymorphs Rutileand Anatase. *J. Mater. Chem.* **1997**, *7* (3), 563–568. https://doi.org/10.1039/a606353e.

(71) Wang, Y.; Sun, T.; Liu, X.; Zhang, H.; Liu, P.; Yang, H.; Yao, X.; Zhao, H. Geometric Structure of Rutile Titanium Dioxide (111) Surfaces. *Phys. Rev. B* **2014**, *90* (4),

045304. https://doi.org/10.1103/PhysRevB.90.045304.

TOC

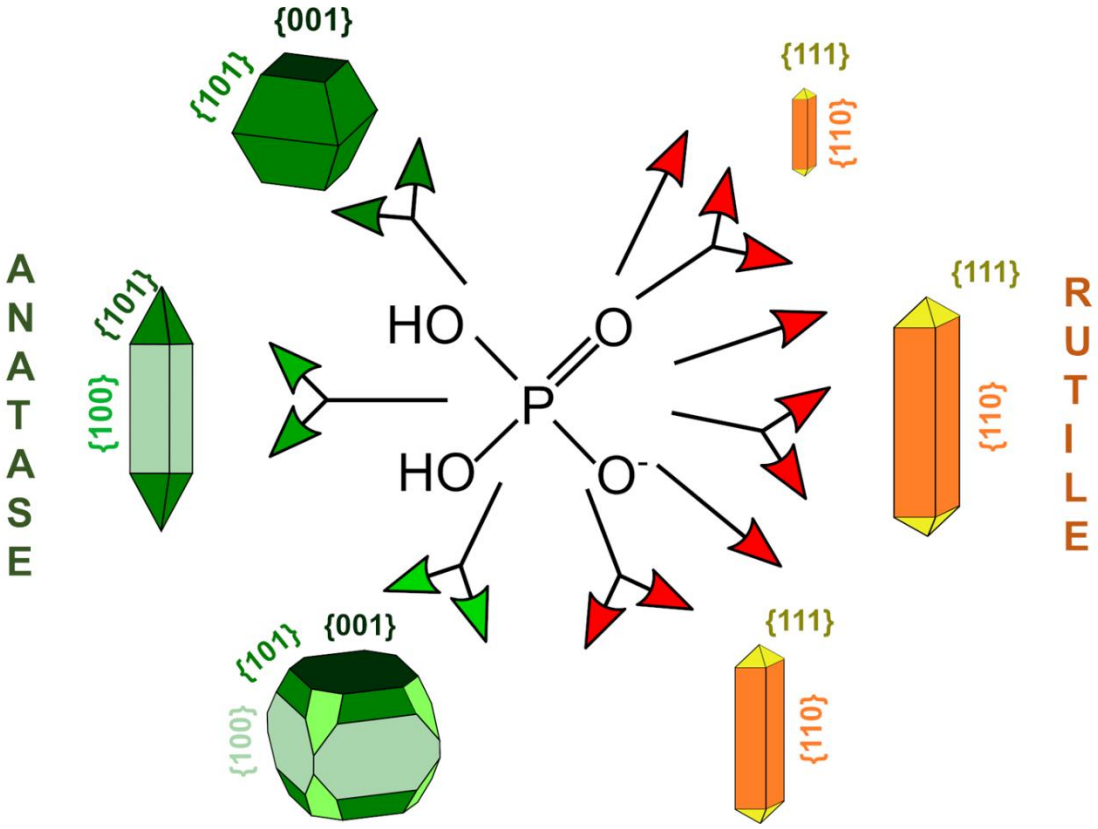
ANATASE
{001}
{101}
{101}
{100}
{001}
{101}
{100}
HO
O
P
HO
O-
{111}
{110}
{111}
{110}
{111}
{110}
RUTILE